J. Fluid Mech. (2008), *vol.* 594, *pp.* 271–305. © 2008 Cambridge University Press
doi:10.1017/S0022112007009056 Printed in the United Kingdom

Interactions of a stationary finite-sized particle with wall turbulence

LANYING ZENG[1], S. BALACHANDAR[1]†, PAUL FISCHER[2]
AND FADY NAJJAR[3]

[1]Department of Theoretical and Applied Mechanics, University of Illinois at Urbana-Champaign,
Urbana, IL 61801, USA

[2] Mathematics and Computer Science Division, Argonne National Laboratory, Argonne, IL 60439, USA

[3] Center for Simulation of Advanced Rockets, University of Illinois at Urbana-Champaign,
Urbana, IL 61801, USA

(Received 16 March 2006 and in revised form 1 September 2007)

Reliable information on forces on a finite-sized particle in a turbulent boundary layer is lacking, so workers continue to use standard drag and lift correlations developed for a laminar flow to predict drag and lift forces. Here we consider direct numerical simulations of a turbulent channel flow over an isolated particle of finite size. The size of the particle and its location within the turbulent channel are systematically varied. All relevant length and time scales of turbulence, attached boundary layers on the particle, and particle wake are faithfully resolved, and thus we consider fully resolved direct numerical simulations. The results from the direct numerical simulation are compared with corresponding predictions based on the standard drag relation with and without the inclusion of added-mass and shear-induced lift forces. The influence of turbulent structures, such as streaks, quasi-streamwise vortices and hairpin packets, on particle force is explored. The effect of vortex shedding is also observed to be important for larger particles, whose *Re* exceeds a threshold.

1. Introduction

Dispersed multiphase flows are common in many engineering and environmental applications. The crucial physics in dispersed multiphase flows is at the interface between phases. Accurate accounting of the deformation of the interface and the exchange of mass, momentum and energy across the interface is essential to both the Eulerian–Lagrangian and Eulerian–Eulerian approaches. For example, the hydrodynamic force on the dispersed phase controls critical processes such as dispersion, preferential accumulation, deposition, resuspension, collision and breakup. The particles in turn modulate the carrier phase through back-coupling of mass, momentum and energy.

In macro-scale formulations of multiphase flow, coupling between the phases is taken into account in terms of correlations for drag coefficient (Schiller & Neumann 1933), lift coefficient (Dandy & Dwyer 1990; Mei 1992) and heat transfer (Ranz & Marshall 1952). Other correlations that attempt to account for additional effects, such as compressibility, evaporation, etc., can be found in Crowe, Sommerfeld & Tsuji

† Present address: Department of Mechanical and Aerospace Engineering, University of Florida, Gainesville, FL 32611, USA.

(1998) and Sirignano (1999). Such empirical correlations have been obtained under simple uniform or linear ambient conditions, where the length and time scales of the ambient flow are much larger than those of the dispersed phase. The accuracy of these empirical correlations is not guaranteed when used beyond the range of validity, especially for finite-sized particles, which are defined as particles of a size comparable to the scales of the carrier phase or larger.

In many applications, the carrier phase is turbulent with eddies of length scale comparable to the particle, and the ambient flow seen by the particle cannot be treated simply as a uniform flow. However, the available experiments lack consensus and suggest Widely varying effects, anywhere from a substantial increase to a dramatic reduction of mean drag by free-stream turbulence (Torobin & Gauvin 1959; Uhlherr & Sinclair 1970; Zarin & Nicholls 1971; Rudolff & Bachalo 1988; Gore & Crowe 1990; Wu & Faeth 1994; Brucato, Grisafi & Montante 1998). Recent computations have somewhat clarified the picture and shown that free-stream isotropic turbulence has little systematic effect on time-averaged mean drag (Bagchi & Balachandar 2003) and thus time-averaged mean forces on the particle can be adequately predicted with the standard drag correlation. The experimental scatter in the effect of free-stream turbulence can be explained in terms of the competing effects of nonlinear dependence of force on relative velocity at higher Reynolds numbers and trajectory bias of particles within the turbulent flow. Although the time-averaged mean can be predicted accurately, it is hard to predict accurately the instantaneous force on the particle with the standard correlation. Especially for particles of size larger than Kolmogorov scale, the departure from standard correlation is significant and chaotic.

Our aim is to understand the influence of wall turbulence on a spherical particle located close to a solid boundary. Several experiments have addressed the problem of particulate wall-bounded flows (Tsuji & Morikawa 1982; Tsuji, Morikawa & Shiomi 1984; Rashidi, Hetsroni & Banerjee 1990; Young & Hanratty 1991; Fessler, Kulick & Eaton 1994; Kaftori, Hetsroni & Banerjee 1995*a*,*b*; Sato & Hishida 1996; Suzuki, Ikenoya & Kasagi 2000; Caraman, Boree & Simonin 2003). Computational efforts have generally been limited to small particles with the use of the point particle assumption (see Brooke, Hanratty & McLaughlin 1994). A significant exception is the work of Pan & Banerjee (1997) who considered a distribution of finite-sized particles in wall turbulence. These investigations have highlighted the influence of near-wall vortical structures on the motion of particles and the pattern of preferential accumulation.

The influence of wall turbulence on the streamwise component of force on the particle can be anticipated to be qualitatively similar to that of free-stream isotropic turbulence. In the case of isotropic turbulence, the important parameters are the ratio of particle diameter to the Kolmogorov length scale and the relative intensity of turbulence with respect to mean relative velocity between the particle and the ambient flow (Bagchi & Balachandar 2004). The inhomogeneous nature of wall turbulence introduces interesting complexity. The relative position of the particle from the nearby wall as compared to the boundary-layer thickness, or the channel half-height, becomes an important parameter. The interaction between the particle and wall turbulence can be expected to be different depending on whether the particle is embedded within the viscous sublayer, buffer region, or the log layer.

The influence of wall turbulence on the wall-normal component of force on the particle is likely to be far more interesting. Although the wall-normal component of force is, in general, significantly weaker than the streamwise component, its influence is important in processes such as deposition, resuspension and wall impaction. The lift force on a particle sitting on the wall in a turbulent boundary layer was originally considered by Hall (1988) and the experimental technique was later improved by Mollinger & Nieuwstadt (1996) to measure instantaneous fluctuating lift force on a particle sitting on the wall in a turbulent boundary layer. Both these measurements reported enhanced lift force, which was much larger than what can be estimated from Saffman's shear-induced lift (Saffman 1965), and even comparable in magnitude to the streamwise drag force. It can be conjectured that as the particle approaches the wall, the lift force on it sharply increases sufficiently close to the wall. Since the mechanisms responsible for such a sharp increase in lift force are not fully explored, it is not clear how close the approach to the wall must be for significantly enhanced lift force to be realized.

Here we report results obtained from direct numerical simulations (DNS) of a finite-sized particle embedded in a fully developed turbulent channel flow. The size and location of the particle within the channel are varied. These are fully resolved numerical simulations, where in addition to resolving the wide range of length and time scales associated with wall turbulence, all the length and time scales associated with the particle and the small-scale flow features generated by it are fully resolved. Merle, Legendre & Magnaudet (2005) considered large-eddy simulation of a turbulent pipe flow over a stationary spherical bubble positioned along the axis of the pipe and it is of interest to compare the present findings for a rigid spherical particle with their results.

In this study, we consider a range of particle sizes from about 2 to 15 times the Kolmogorov scale, in order to assess the importance of particle size relative to flow scales on particle–turbulence interaction. Two different particle positions are considered here. In the first set of simulations, the particle is placed within the buffer region, where turbulence production is at its peak, and thus the particle is expected to have the largest back-effect on carrier phase turbulence. In the buffer region, the near-wall vortical structures are most active and it is of interest to investigate their influence on the particle. Furthermore, the largest particle considered extends almost into the viscous sublayer and it will be of interest to see whether significantly enhanced lift forces similar to those observed by Hall (1988) and Mollinger & Nieuwstadt (1996) are realized. In the second set of simulations, the particle is placed along the channel centre, where the wall effect is minimal, and the carrier phase can be considered as nearly isotropic turbulence. Thus, the second set can be compared against the investigation of particle interaction with free-stream isotropic turbulence by Bagchi & Balachandar (2003, 2004). In all the cases, the particle is maintained fixed in position as the turbulent channel flow passes by. Although there are applications where turbulent flow over a fixed particle is of interest, in many multiphase problems the particle is in motion. The simpler case of a frozen particle is clearly the first step before addressing the more complex situation of a particle in free motion in wall turbulence.

The objectives of the present study are as follows. (i) Detailed experimental measurement of forces on an individual particle located within wall turbulence is hard to accomplish and as a result high-quality data is scarce. Here through DNS we will obtain detailed information on instantaneous force on a rigid stationary particle in a turbulent channel flow. Different particle sizes and different particle locations within the channel will be considered. (ii) The adequacy of standard drag correlation in accurately predicting mean and fluctuating components of force on the particle will be evaluated. (iii) The effect of including added mass, pressure gradient and lift contributions in force estimation will be explored. (iv) The interaction of near-wall turbulent structures, such as high- and low- speed streaks, hairpin packets and quasi-streamwise vortices, with the particles and their influence on instantaneous force will be explored. (v) For larger particles, the effect of self-induced vortex shedding and the resulting stochastic contribution to lift force will be investigated.

2. Problem description and methodology

We consider a fully developed turbulent channel flow between two infinite smooth parallel plates, characterized by a single non-dimensional parameter: Reynolds number based on channel half-height (H) and friction velocity (u_τ). Here we consider a modestly turbulent channel flow with $Re_\tau = Hu_\tau/\nu = 178.12$ (ν is the kinematic viscosity of the fluid), which has been extensively studied since the pioneering work of Kim, Moin & Moser (1987). A rigid stationary spherical particle of diameter, d, is located within the channel at a distance y_p from the bottom wall. The diameter of the particle and the distance from the wall in wall units are defined as $d_+ = du_\tau/\nu$ and $y_{p+} = y_p u_\tau/\nu$, respectively.

In this study, we consider a range of particle diameters varying from about 3.5 to 25 wall units, placed either within the buffer region at a distance $y_{p+} = 17.81$ from the bottom wall or along the channel centre at $y_{p+} = 178.12$. When placed in the buffer layer, the smallest particle is entirely within the buffer region, while the largest particle extends almost into the viscous sublayer. For the largest particle ($d_+ = 24.94$), the gap between the bottom of the particle and the bottom wall is only 5.34 wall units.

In wall units, the Kolmogorov length scale (η) can be written in terms of local dissipation rate as $\eta_+ = \eta u_\tau/\nu = \epsilon_+^{-1/4}$. The dissipation rate increases monotonically from the centre to the channel walls and accordingly at $Re_\tau = 178.12$ the Kolmogorov length scale is the lowest ($\eta_+ = 1.55$) close to the wall and reaches a maximum at the channel centre-plane ($\eta_+ = 3.70$). At $y_{p+} = 17.81$, the diameter of the particle is varied from about 2.0 to 14.3 times the local Kolmogorov scale, whereas at the channel centre the diameter of the particle is chosen to be 4.8 and 6.7 times the local Kolmogorov scale. Since the particle is fixed in space, the instantaneous relative velocity is simply the local fluid velocity and thus the mean (time-averaged) particle Reynolds number is given by $Re = \langle u^*(y_{p*})\rangle d/\nu = \langle u_+(y_{p+})\rangle d_+$, where the asterisk indicates a dimensional quantity and angle brackets represent ensemble average. The mean particle Reynolds number is generally lower at $y_{p+} = 17.81$ and the particle Reynolds number ranges from 42 to 295. At the channel centre, owing to increased mean flow velocity, the particle Reynolds number is larger and $Re \approx 325$ and 455 for the two different particle sizes. Since the particle is held fixed, the ratio of ambient r.m.s. velocity fluctuation (u_{rms}) to mean fluid velocity seen by the particle ($\langle u\rangle$) is only a function of particle location and the ratio is 23.16 % and 4.09 % at $y_{p+} = 17.81$ and $y_{p+} = 178.12$, respectively. Thus the particles placed in the buffer layer experience intense turbulence, while those at the centreline see only weak turbulent fluctuations. The details of the six cases considered can be found in table 1.

The height of the channel in wall units is $2Re_\tau$. Along the spanwise (z) direction, periodic boundary conditions are employed and the spanwise extent of the computational domain is $4\pi/3$ times the half-channel height, which is a standard choice in turbulent channel-flow simulations (Kim *et al.* 1987). The cross-sectional area of the largest particle under consideration is only 0.18 % of the total channel cross-section. For the smallest particle, the cross-sectional area is two orders of magnitude smaller and thus in all cases considered, the blockage effect due to the

Case	d_+	d/η	y_{p+}	$u_{rms}/\langle u\rangle$	Re
1	3.56	2.0	17.81	23.16 %	42
2	10.69	6.1	17.81	23.16 %	125
3	17.81	10.2	17.81	23.16 %	210
4	24.94	14.3	17.81	23.16 %	295
5	17.81	4.8	178.1	4.09 %	325
6	24.94	6.7	178.1	4.09 %	455

TABLE 1. Parameters for the simulation.

particle is negligible. The streamwise (x) extent of the computational domain is chosen to be 2.4 times the half-channel height. A fully developed turbulent channel flow is applied as inflow at the upstream streamwise inlet end of the computational domain. A simple convective outflow boundary condition is applied at the other end.

In turbulent channel-flow simulations (without the particle), it is customary to choose a long streamwise domain with periodic boundary conditions (Kim *et al.* 1987). The assumption of periodicity in these simulations requires the streamwise size of the domain to be sufficiently longer than the streamwise correlation length and a domain of length 4π times the half-channel height is typically chosen.

Here we perform two simultaneous simulations. The first is a standard turbulent channel-flow simulation at $Re_\tau = 178.12$ in a streamwise periodic domain of streamwise length 4π times the half-channel height. The second is the inflow-outflow channel-flow simulation with the embedded particle, whose streamwise length has been described above as 2.4 times the half-channel height. The wall-normal-spanwise (y–z) cross-section of the two computational domains match, and the second domain with the embedded particle is placed downstream of the first periodic domain. At each time, the fully developed turbulent channel velocity field obtained at the downstream (y, z)-plane of the periodic domain is applied as the inflow boundary condition for the second domain that includes the particle.

In § 2.2, we demonstrate that the channel-flow turbulence simulated in the periodic domain is accurately evolved in the inflow–outflow simulation and that the various statistics of channel-flow turbulence obtained in the downstream domain are identical to those obtained in the upstream periodic domain. Furthermore, in the inflow–outflow simulation, the distances from the particle centre to the upstream and downstream boundaries have been chosen to be equal to 0.8 and 1.6 times the half-channel height. These upstream and downstream distances are several times the particle diameter, even for the largest particle considered. Thus, the domain is adequate for capturing fully the disturbance flow generated by the presence of the particle. These turbulent inflow simulations are similar in spirit to those in the context of free-stream isotropic turbulence (Bagchi & Balachandar 2003, 2004).

The turbulent channel-flow simulation in a streamwise periodic domain is an auxiliary simulation, whose purpose is to provide an accurate inflow for the simulation with the embedded particle. For the auxiliary simulation, we employ the standard Fourier–Fourier–Chebyshev spectral methodology. The resolution along the streamwise, spanwise and wall-normal directions are $128 \times 128 \times 128$, which is more than adequate for the present case of $Re_\tau = 178.12$ (Kim *et al.* 1987). Despite the larger domain, the computational cost of the auxiliary simulation is only a fraction of that of the inflow–outflow simulation with the embedded

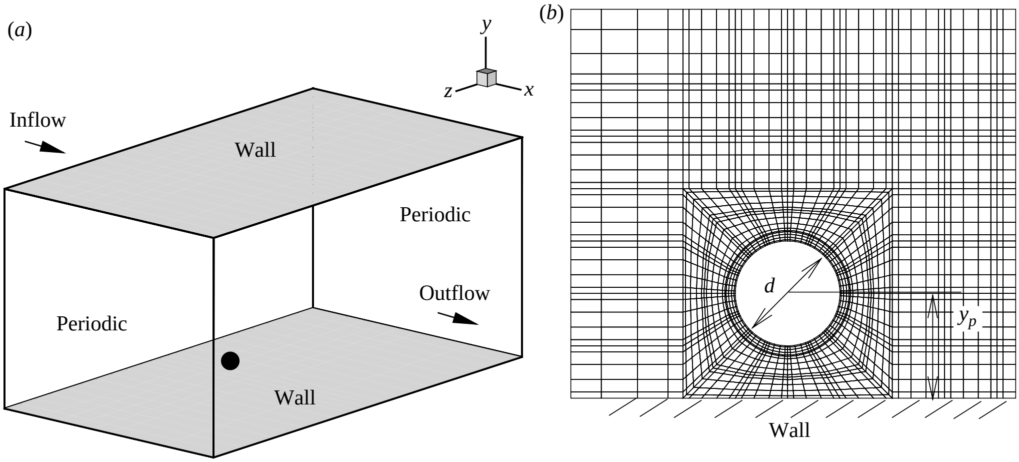

FIGURE 1. Sample spectral element discretization of the computational domain for the $y_{p+} = 17.81$ case. (*a*) The particle in relation to the entire computational box; only the spectral element discretization is shown. (*b*) The bounding box around the particle where the spectral element discretization transitions from the sphere to a box. Sub-element Gauss–Lobatto discretization is also shown.

particle. Thus, the combination of auxiliary turbulent channel-flow simulation in a long streamwise-periodic domain with the inflow–outflow simulation in a shorter streamwise domain with an embedded particle, provides an accurate and efficient framework for investigate particling wall–turbulence interaction. This approach is computationally more effective than a simulation involving one long streamwise domain that includes the particle.

2.1. *Numerical methodology*

The present simulations employ spectral element methodology (SEM), (Deville, Fischer & Mund 2002) and an existing SEM code (Nek5000) has been used. The computational domain is partitioned into hexahedral elements and within each element, velocity and pressure are represented in local Cartesian coordinates by tensor-product Lagrange polynomials of degree N and $N-2$, respectively. Time stepping is based on a semi-implicit splitting scheme that, with correct treatment of the incompressibility constraint, allows high-order temporal accuracy. The results reported here employ 3400 spectral elements with each element resolved by $11 \times 11 \times 11$ Legendre–Gauss–Lobatto points. The present inflow–outflow simulations thus employ 3.4 million points, which can be compared with the 2.1 million points used for the standard $(128)^3$ streamwise-periodic turbulent channel-flow simulation. Because of the shorter streamwise domain, the effective resolution of the inflow–outflow simulation is about eight times finer than the corresponding channel-flow simulation.

A three-dimensional view of the grid is shown in figure 1. Except within a small bounding box around the particle, the hexahedral elements are rectangular in shape. Within the bounding box, the hexahedral elements deform from the outer box to the inner sphere. It is important to point out that the spherical surface of the particle is represented accurately as a tenth-order polynomial and not as a patchwork of flat surfaces. The isoparametric mapping helps in the transition from the spherical surface to the Cartesian mesh away from the sphere. The detailed mesh within the bounding box around the particle is also shown in figure 1.

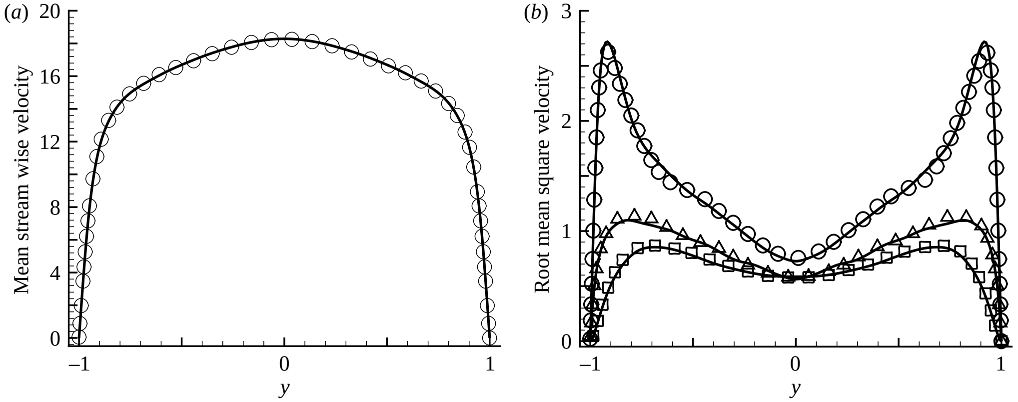

FIGURE 2. Velocity profiles along wall-normal direction. (*a*) Mean streamwise velocity; (*b*) r.m.s. of streamwise, wall–normal and spanwise components. ——, channel with spectral element method for $N = 11$; symbols, fully spectral channel flow. ○, streamwise; □, wall-normal; △, spanwise.

2.2. *Resolution*

The first task is to establish the accuracy of the inflow–outflow simulation and its ability to faithfully reproduce the turbulent channel-flow statistics. The spectral element grid away from the particle must be such that it can adequately resolve all the scales of turbulent channel flow. The region away from the particle is discretized with 7, 20 and 22 spectral elements along the streamwise, wall-normal and spanwise directions, which for $N = 11$ yield effectively 71, 201 and 221 grid points along the three directions. In order to accommodate the bounding box around the particle, the spectral elements are chosen to be of non-uniform width and furthermore the Gauss–Lobatto grid within the elements is non-uniformly distributed. For $N = 11$, the smallest and the largest grid spacings in wall units are 1.176 and 15.804 along the streamwise direction and 0.705 and 5.427 along the spanwise direction. In comparison, the discretization of the $(128)^3$ fully spectral channel-flow simulation are 17.487 and 5.829 along the streamwise and spanwise directions. Along the wall-normal direction, the spectral element grid varies from a very fine spacing of 0.0529 wall units near the wall to a larger grid spacing of 4.214 near the channel centre. The corresponding fully spectral grid is also non-uniform along the wall-normal direction and it varies from 0.054 to 4.371 from the channel wall to the centreline. So the spectral element grid is finer than the fully spectral channel-flow grid over the entire computational domain. In fact, this is the basic requirement that guided the present choice of distribution of spectral elements and the sub-element resolution. Note that with $N = 11$, the spectral element simulation offers tenth-order accuracy and thus with the present fine grid we expect the resolution to be comparable to a fully spectral simulation.

Before the study of particle–wall turbulence, we first performed a turbulent inflow–outflow channel simulation in the absence of the particle with the spectral element code. The grid resolution over the bulk of the channel is maintained the same as that for the simulation with the particle, to allow us to establish the adequacy of the spectral element grid in resolving all the scales of turbulent channel flow. We compare the mean streamwise velocity obtained from the spectral element simulation with that from the fully spectral simulation (figure 2*a*). Also compared are the r.m.s. velocity fluctuations (figure 2*b*). The statistics have also been thoroughly compared

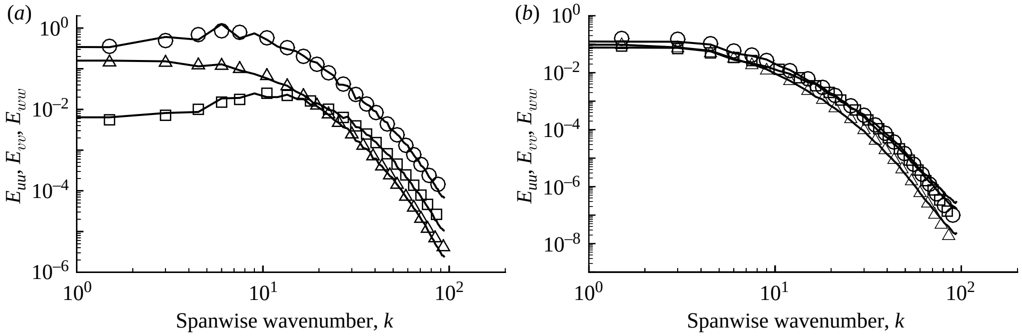

FIGURE 3. Spanwise spectra of streamwise, wall-normal and spanwise velocities. (*a*) ——, spectra obtained at $y_+ = 18.7$ with the spectral element simulation using $N = 11$; symbols (same as figure 2): spectra obtained at $y_+ = 19.02$ from a fully spectral simulation for $ny = 128$; (*b*) same as (*a*), but spectra obtained at channel centre ($y_+ = 178.12$).

with the classic channel flow data of Kim *et al.* (1987). The agreement in both the mean and r.m.s. velocities is good, indicating the adequacy of the present spectral element grid. The observed small differences are due to the finite length over which the time-average has been performed.

We also compare spanwise spectra of streamwise, wall-normal and spanwise velocities, obtained from the spectral element simulation with those from the fully spectral simulation (figure 3). The comparisons are made at two different locations, one in the buffer region ($y_{p+} = 18.7$) and the other at channel centre ($y_{p+} = 178.12$). The agreement is good over the entire spectra, indicating that all the turbulent scales are well resolved by the spectral element simulation. Detailed flow fields at various locations are also compared systematically, and they show excellent agreement between the inflow–outflow spectral element simulation and the streamwise-periodic fully spectral simulation, which again guarantees the adequacy of the present spectral element grid.

The spectral element simulation uses a shorter streamwise length with turbulent channel flow applied as inflow. In order to verify the appropriateness of this approach, the spanwise spectra shown in figure 3 were computed at different streamwise locations in the spectral element code and the results are remarkably similar (and therefore not shown here) indicating that the inflow turbulence is well maintained within the computed channel length.

The resolution around the particle uses 384 surface elements and with $N = 11$ yields a total of 38 400 grid points around the sphere. The first layer of grid points away from the surface of the particle is at a radial distance of $\Delta r_+ = 0.059$. This choice of resolution close to the particle has been guided by our prior experience with this code in solving wall-bounded flows over a sphere (Zeng, Balachandar & Fischer 2005). The chosen grid around the particle is more than adequate for resolving all the boundary-layer dynamics around the particle over the Reynolds-number range under consideration here.

The simulations with the particle required a fine time step of $\Delta t_+ = \Delta t/(\nu/u_\tau^2) = 1.78 \times 10^{-3}$. Once the flow has reached a statistically stationary state, simulations were continued for about 285 non-dimensional time units in order to collect accurate time-averaged statistics. The simulations are thus computationally expensive and were typically performed on 256 processors of an IBM-SP5. Each simulation required nearly 1.3 months of computations on the 256 processors.

3. Results

3.1. *Mean and fluctuating forces*

The instantaneous force on the particle is evaluated by integrating the non-dimensional pressure and viscous stresses around the surface of the particle (S) as

$$\boldsymbol{F}_{DNS}=\frac{\boldsymbol{F}^{*}}{\rho u_{\tau}^{2}H^{2}}=\int_{S}(-p\boldsymbol{n}+\boldsymbol{n}\cdot\boldsymbol{\tau})\,\mathrm{d}s, \tag{3.1}$$

where $\boldsymbol{F}^{*}$ is the dimensional force on the particle, p and $\boldsymbol{\tau}$ are the non-dimensional pressure and viscous stress tensor computed in the DNS and $\boldsymbol{n}$ is the outward unit normal to the surface of the particle and $\boldsymbol{F}_{DNS}$ is the non-dimensional force normalized with $\rho u_{\tau}^{2}H^{2}$ as the force scale. The streamwise (x), wall-normal (y) and spanwise (z) components of the instantaneous force obtained from the simulations will be presented below. We will also present the force predicted using the standard drag relation,

$$\boldsymbol{F}_{std}=\frac{\pi}{8}C_{D}\frac{d_{+}^{2}}{Re_{\tau}^{2}}|\boldsymbol{u}_{+}|\boldsymbol{u}_{+}, \tag{3.2}$$

where the drag coefficient is given in terms of particle Reynolds number as

$$C_{D}=\frac{24}{Re}(1+0.15Re^{0.687})\quad\text{where}\quad Re=\frac{|\boldsymbol{u}^{*}|d}{\nu}. \tag{3.3}$$

The above prediction is based on instantaneous relative velocity as seen by the particle. For the present case of a stationary particle, in (3.3), $\boldsymbol{u}_{+}$ is the instantaneous undisturbed fluid velocity as seen by the particle, whose estimation will be discussed below.

3.1.1. *Undisturbed fluid velocity*

The estimation of undisturbed fluid velocity in a numerical simulation, which includes an embedded particle is not straightforward, since the flow has already been disturbed. Furthermore, for a finite-sized particle there remains a question, where should the undisturbed fluid velocity be estimated? It can be taken as the undisturbed fluid velocity at the particle centre or can be approximated as a volume average over the finite-sized particle, and so on. In their investigation of a frozen cubic box of isotropic turbulence passing over a particle, Bagchi & Balachandar (2003) knew precisely the precomputed undisturbed turbulence over the entire box. The undisturbed fluid velocity at the location of particle centre was observed to be a good choice for $\boldsymbol{u}_{+}$. Merle *et al.* (2005) used the Taylor hypothesis to approximate $\boldsymbol{u}_{+}$ to be the fluid velocity of an upstream point at an earlier time. In the present simulations, we strictly take $\boldsymbol{u}_{+}$ to be the undisturbed fluid velocity at the particle centre. Identical inflow–outflow simulations were performed with turbulent inflow, but without the embedded particle. The fluid velocity thus obtained in the absence of the particle, evaluated at the point where the particle centre would have been, is taken as $\boldsymbol{u}_{+}$.

The above definition is based on instantaneous undisturbed fluid velocity at the location of the particle centre. It can be anticipated that this definition is adequate as the diameter of the particle becomes smaller than the length scales of the flow. In the present simulations we will later observe that this definition is adequate for the smallest particle ($d_{+}=3.56$) in predicting the instantaneous force. For larger particles, the use of undisturbed fluid velocity evaluated at the centre of the particle can be questioned. Instead, the fluid velocity seen by the particle can be approximated by a weighted volume average of undisturbed local fluid velocity over a small sphere of radius a centred around the particle location, $\boldsymbol{x}_{p+}$, as

$$\boldsymbol{u}_{+,avg} = \int_{|\boldsymbol{r}_+|<a} \boldsymbol{u}_+(\boldsymbol{x}_{p+} + \boldsymbol{r}_+, t_+) G(\boldsymbol{r}_+)\, \mathrm{d}\boldsymbol{r}_+, \tag{3.4}$$

where $G(\boldsymbol{r}_+)$ is a filter function and it satisfies $\int_{|\boldsymbol{r}_+|<a} G(\boldsymbol{r}_+)\mathrm{d}\boldsymbol{r}_+ = 1$. In case of a simple volume average, G can be chosen to be a top-hat function. Instead, using Taylor's hypothesis, the fluid velocity seen by the particle can also be defined as a weighted time average over a time interval $2b$:

$$\boldsymbol{u}_{+,avg} = \int_{|\tau_+|<b} \boldsymbol{u}_+(\boldsymbol{x}_{p+}(t_+ + \tau_+), t_+ + \tau_+) G(\tau_+)\, \mathrm{d}\tau_+. \tag{3.5}$$

The later definition is far more convenient to implement in the context of tracking point particles in turbulent flow. However, in this case, the filter function must weigh only the past velocity seen by the particle, as the future position of the particle remains to be solved. In the present context, the above modified definitions of undisturbed fluid velocity seen by the particle have been tested for a range of filter widths. These modified definitions of fluid velocity do not alter the standard drag prediction noticeably, provided $a \approx d_+$ or $b \approx d_+/\langle u_+(y_{p+})\rangle$. Clearly, as the domain of integration (a or b) is increased, the level of fluctuation in the predicted force decreases, but comparison with the actual instantaneous force does not improve. Bagchi & Balachandar (2003) also found that the volume averaged definition of undisturbed fluid velocity seen by the particle does not improve the standard drag prediction in the context of a particle subjected to isotropic free-stream turbulence. Thus, all the results to be reported here will be based on $\boldsymbol{u}_+$ approximated at the particle centre.

3.1.2. *Small particle ($d_+ = 3.56$)*

Figure 4 presents the results computed for the smallest particle ($d_+ = 3.56$) placed within the buffer region ($y_{p+} = 17.81$). It is clear that the force on the particle shows substantial variation in time and the r.m.s. force fluctuation is nearly 27.7 % of the mean. For the smallest particle under consideration, the standard drag model captures very well the time evolution of the force. The estimation is quite good even without accounting for the added-mass, history and lift forces on the particle, suggesting that their contributions are negligible for such small particles. Furthermore, the non-zero instantaneous wall-normal and spanwise forces are primarily due to the drag force on the particle as the magnitude and direction of ambient flow varies around the particle. The mean wall-normal and spanwise fluid velocities are zero in a channel and as a result the mean wall-normal and spanwise forces on the particle are nearly zero. At $y_+ = 17.81$, the r.m.s. fluctuation in the streamwise, wall-normal and spanwise components of the fluid velocity are in the ratio of 1:0.033:0.46. We observe the r.m.s. fluctuation in the streamwise, wall-normal and spanwise forces on the particle to be in the ratio of 1:0.11:0.30. The wall-normal force fluctuation is proportionately almost three times larger than the wall-normal velocity fluctuation. This underscores the nonlinear relation between force and velocity, and the inter-coupling between the streamwise, wall-normal and spanwise components.

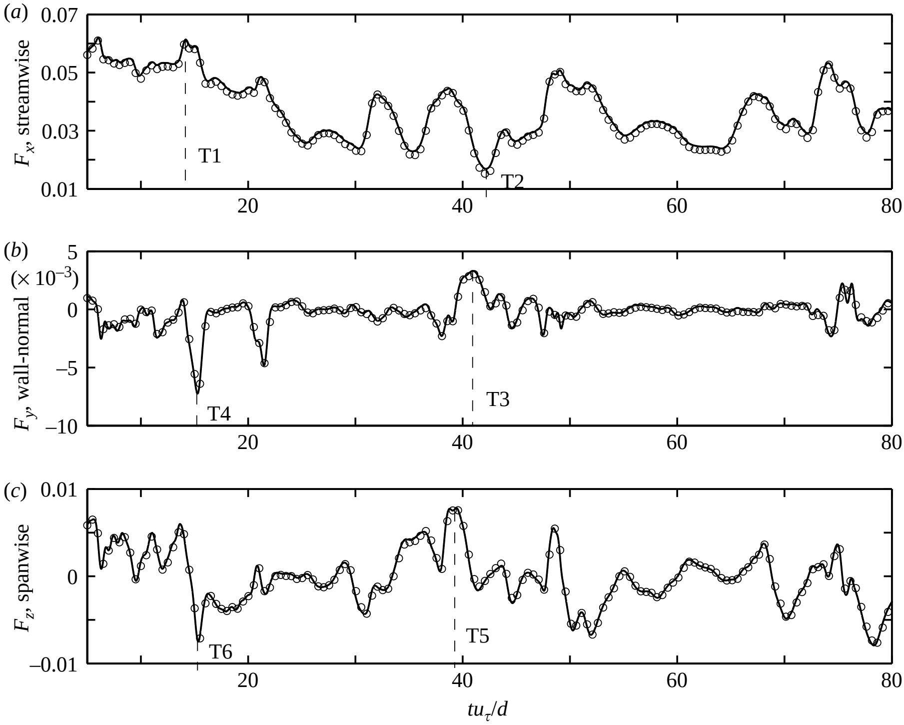

FIGURE 4. Time history of the force components for $d_+ = 3.56$, $y_{p+} = 17.81$. (*a*) Streamwise force; (*b*) wall-normal force; (*c*) spanwise force. ——, present DNS results; ○, forces predicted using the standard drag formulation.

In order to interpret the above observation better, (3.2) and (3.3) can be combined and the predicted force based on standard drag relation can be expressed as

$$\boldsymbol{F}_{std} = \frac{3\pi d_+}{Re_\tau^2}\boldsymbol{u}_+(1 + 0.15 d_+^{0.687}|\boldsymbol{u}_+|^{0.687}). \tag{3.6}$$

For the sake of argument, first consider the ambient flow to be time varying, but unidirectional. We can then express $\boldsymbol{u}_+ = \langle \boldsymbol{u}_+ \rangle (1 + \xi(t))$, where the angle brackets indicate an ensemble average. Here $\xi(t)$ accounts for the time variation and by definition $\langle \xi \rangle = 0$ and $\langle \xi^2 \rangle^{1/2} = u_{+,rms}/|\langle \boldsymbol{u}_+ \rangle|$. The corresponding force on the particle is also time varying and is in the direction of the unidirectional flow. If we assume the ambient velocity fluctuations to be small (i.e. $\xi \ll 1$), then the mean force on the particle can be expressed as follows

$$\langle \boldsymbol{F}_{std} \rangle = \frac{3\pi d_+}{Re_\tau^2}\langle \boldsymbol{u}_+ \rangle [1 + 0.15 d_+^{0.687}|\langle \boldsymbol{u}_+ \rangle|^{0.687}(1 + 0.579\langle \xi^2 \rangle + \text{h.o.t.})], \tag{3.7}$$

and the corresponding r.m.s. force fluctuation can be approximated as

$$F_{std,rms} = \langle (\boldsymbol{F}_{std} - \langle \boldsymbol{F}_{std} \rangle)\cdot(\boldsymbol{F}_{std} - \langle \boldsymbol{F}_{std} \rangle)\rangle^{1/2} \tag{3.8}$$

$$= \frac{3\pi d_+}{Re_\tau^2} u_{+,rms}(1 + 0.253 d_+^{0.687}|\langle \boldsymbol{u}_+ \rangle|^{0.687}). \tag{3.9}$$

The effect of nonlinearity is to increase the mean force on the particle. This can be readily seen by comparing (3.7) with the estimate that a steady ambient flow of

Case		DNS	standard	std+Auton	std+Saffman	std+Mei	std+KK
1	$\langle F_y \rangle$	-2.3658×10^{-4}	-2.7983×10^{-4}	9.6080×10^{-4}	3.4535×10^{-4}	-2.1927×10^{-4}	-2.8218×10^{-4}
1	F'_y	0.0012	0.0012	0.0014	0.0013	0.0012	0.0012
2	$\langle F_y \rangle$	−0.0011	0.0035	0.0360	0.0210	0.0087	0.0013
2	F'_y	0.0109	0.0082	0.0264	0.0199	0.0101	0.0092
3	$\langle F_y \rangle$	−0.0137	0.0068	0.1583	0.0881	0.0482	−0.0208
3	F'_y	0.0300	0.0183	0.1313	0.0858	0.0559	0.0401
4	$\langle F_y \rangle$	−0.0079	0.0026	0.5197	0.2822	0.2042	−0.088
4	F'_y	0.0608	0.0298	0.3883	0.2499	0.2209	0.0647
5	F'_y	0.0648	0.0264	0.0506	0.0284	0.0268	0.0261
6	F'_y	0.1506	0.0477	0.1273	0.0554	0.0500	0.0466

TABLE 2. Mean and r.m.s. of wall-normal component of force for the six different cases. The results computed from the DNS can be compared against prediction with the standard (std) drag correlation plus lift force as given in formulations by Auton (1987), Saffman (1965), Mei (1992) and Kurose & Komori (1999).

magnitude $\langle \boldsymbol{u}_+ \rangle$ would only result in a steady force of

$$\frac{3\pi d_+}{Re_\tau^2}\langle \boldsymbol{u}_+ \rangle [1 + 0.15 d_+^{0.687}\, |\langle \boldsymbol{u}_+ \rangle|^{0.687}]. \tag{3.10}$$

In the context of gravitational settling of a particle, this increase in drag force owing to the nonlinear force–velocity relation is known to result in a reduction in mean settling velocity (Mei 1994).

From (3.6), the mean wall-normal and spanwise forces can be expressed as

$$\langle F_y \rangle = \frac{0.45\pi d_+^{1.687}}{Re_\tau^2}\langle u_{y+} |\boldsymbol{u}_+|^{0.687} \rangle, \quad \langle F_z \rangle = \frac{0.45\pi d_+^{1.687}}{Re_\tau^2}\langle u_{z+} |\boldsymbol{u}_+|^{0.687} \rangle. \tag{3.11}$$

By symmetry argument it can be shown that $\langle u_{z+} |\boldsymbol{u}_+|^{0.687} \rangle = 0$ and as a result the mean spanwise force is expected to be zero. In contrast, $\langle u_{y+} |\boldsymbol{u}_+|^{0.687} \rangle$ need not be zero in the buffer region. As a result, even though mean wall-normal velocity is zero, due to the nonlinear force–velocity relation, the mean wall-normal component of the drag force may not be zero. The mean and r.m.s. wall-normal force ($\langle F_y \rangle$ and F'_y) are presented in table 2 and it can be seen that for the smallest particle, the mean wall-normal component is quite small, especially when compared to the streamwise force. However, both the computed DNS results and the prediction based on standard drag, yield a small negative y-force directed towards the wall.

Experimental measurement of wall-normal force on a stationary particle located in the buffer region is rare; but the present results can be compared with the measurements of Mollinger & Nieuwstadt (1996), who considered lift force on a particle sitting on the wall in a turbulent boundary layer. Their expression for mean lift force on a 120 μm particle can be recast as follows:

$$\langle F_y \rangle_{MN} = 56.9 \frac{1}{Re_\tau^2}\left(\frac{d_+}{2}\right)^{1.87}, \tag{3.12}$$

which was observed to fit their data very well over the range $0.8 \leqslant d_+ \leqslant 4.0$. The present small particle ($d_+ = 3.56$) is clearly in this range. For this particle, (3.12) yields $\langle F_y \rangle_{MN} = 5.2 \times 10^{-3}$, which can be compared with a value of -2.37×10^{-4} obtained in the present simulation. The measured lift force on a particle sitting on the wall is more than an order of magnitude larger than that obtained in the present simulation and is directed in the opposite direction. It thus appears that as the particle is moved from touching the wall ($y_{p+} = 1.78$) to the buffer region ($y_{p+} = 17.81$), the mean drag decreases dramatically and reverses direction. The simulations Zeng (2007) of particle in a wall-bounded linear shear flow illustrate the rapid increase in lift force as the particle approaches the wall and offer a plausible explanation for the observed difference between a particle placed on the wall *vs.* in the buffer region.

As can be seen in (3.9), the effect of nonlinear drag law is to increase the r.m.s. force fluctuation as well. According to (3.9), the r.m.s. force fluctuation along any three mutually perpendicular directions is proportional to r.m.s. velocity fluctuation along those directions. This behaviour is contrary to that observed in the present simulation and the discrepancy is clearly due to fluctuation in both magnitude and direction of the ambient velocity seen by the particle. From (3.6), it can readily be seen that even when wall-normal velocity fluctuations are weak, fluctuation in the other two components can result in disproportionate wall-normal force fluctuation. It can be interpreted as the strong fluctuation in the streamwise and spanwise velocity components, through their influence on the particle Reynolds number, contributing to enhanced wall-normal force fluctuation. Furthermore, it is observed that the streamwise force fluctuations are relatively more amplified than the spanwise component and this perhaps is due to the increased nonlinearity for the streamwise component owing to presence of a non-zero mean contribution.

3.1.3. *Larger particles*

The results for the three larger particle sizes are shown in figures 5, 6 and 7. Both the DNS result and the standard drag prediction are plotted for the three components. The corresponding mean and r.m.s. values are presented in figure 8. In all cases, the time-averaged mean streamwise force is more than an order of magnitude larger than the wall-normal and spanwise components. The mean streamwise force steadily increases with particle size. By symmetry argument, we expect the long-time average of the spanwise fluid velocity to be zero and, correspondingly, the long, time average of the spanwise force on the particle to be zero as well. The small non-zero values in the present simulations are due to finite time average.

The computed time-averaged wall-normal force remains negative (wallward) in all cases considered. The mean wall-normal force is small for the two smaller particles. For particles of size $d_+ = 17.81$ and 24.94, the mean wall-normal force is larger and of sufficient magnitude to be relevant. As discussed above, although the long-time average of the wall-normal velocity is zero, there can be a non-zero mean wall-normal force arising from only the drag consideration. In addition, for the larger particles, contribution from shear and wall-induced lift mechanisms can contribute to the wall-normal force.

We first obtain an estimate for the contribution to mean wall-normal force that arises as a result of the nonlinear drag relation. Let us split the instantaneous undisturbed fluid velocity seen by the particle into a mean and a fluctuating component as $\boldsymbol{u}_+ = \langle \boldsymbol{u}_+ \rangle + \boldsymbol{u}_+'$. Note that the mean undisturbed flow at the particle centre, $\langle \boldsymbol{u}_+ \rangle$, is along the streamwise direction and, as can be seen in figure 2, the velocity fluctuations are five to ten times smaller than the mean in the buffer region. Substituting for $\boldsymbol{u}_+$ in terms of mean and perturbation and expanding in the small parameter, $\boldsymbol{u}_+'/\langle \boldsymbol{u}_+ \rangle$

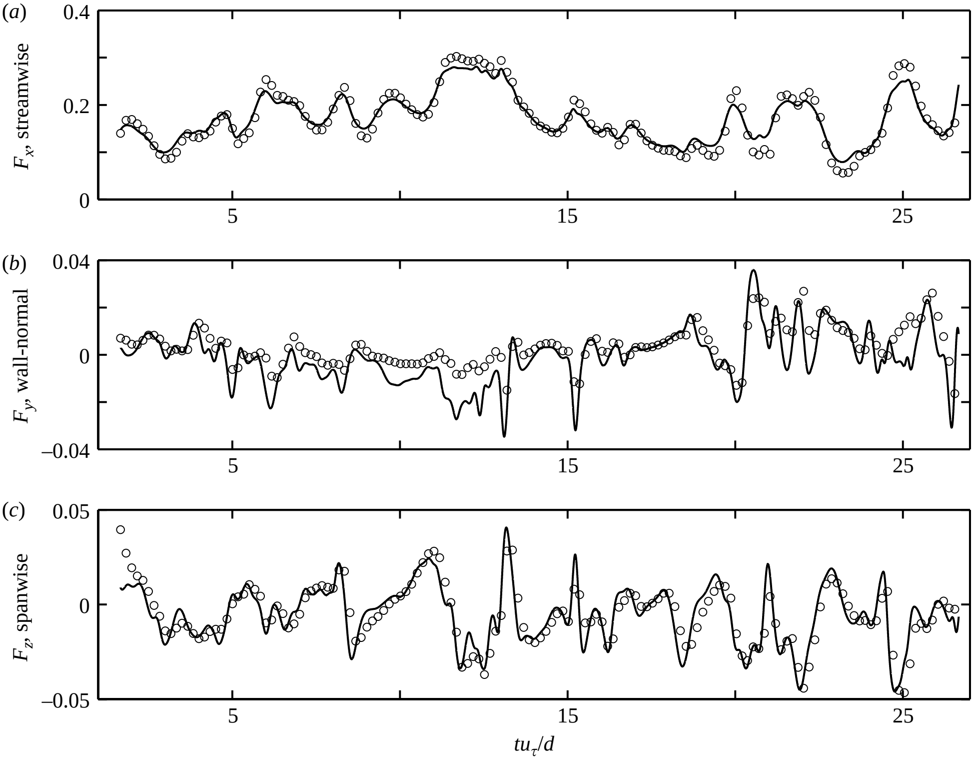

FIGURE 5. Same as figure 4 for $d_+ = 10.69$, $y_{p+} = 17.81$.

we obtain

$$|\boldsymbol{u}_+|^{0.687} = |\langle \boldsymbol{u}_+ \rangle|^{0.687}\left[1 + 0.687\frac{u'_{x+}}{|\langle \boldsymbol{u}_+ \rangle|} - 0.108\left(\frac{u'_{x+}}{|\langle \boldsymbol{u}_+ \rangle|}\right)^2 + 0.3435\left(\left(\frac{u'_{y+}}{|\langle \boldsymbol{u}_+ \rangle|}\right)^2 + \left(\frac{u'_{z+}}{|\langle \boldsymbol{u}_+ \rangle|}\right)^2\right) + \text{h.o.t.}\right], \quad (3.13)$$

where u'_{x+}, u'_{y+} and u'_{z+} are the streamwise, wall-normal and spanwise components of the fluctuation and h.o.t. represents higher-order terms. Substituting the above into (3.11), the mean wall-normal force can be expressed in terms of perturbation velocity correlations as

$$\langle F_y \rangle = \frac{0.31\pi d_+^{1.687}\,|\langle \boldsymbol{u}_+ \rangle|^{1.687}}{Re_\tau^2}\left[\frac{\langle u'_{x+}u'_{y+} \rangle}{|\langle \boldsymbol{u}_+ \rangle|^2} - 0.16\frac{\langle u'^2_{x+}u'_{y+} \rangle}{|\langle \boldsymbol{u}_+ \rangle|^3} + \frac{1}{2}\frac{\langle u'^3_{y+} \rangle}{|\langle \boldsymbol{u}_+ \rangle|^3} + \frac{1}{2}\frac{\langle u'^2_{z+}u'_{y+} \rangle}{|\langle \boldsymbol{u}_+ \rangle|^3}\right]. \quad (3.14)$$

The contribution from the different terms can be explored. The first term, which is quadratic in the fluctuation, is likely to make a larger contribution than the other terms, which are cubic in the fluctuation. In the bottom half of the channel, the Reynolds shear stress, $\langle u'_{x+}u'_{y+} \rangle$, is negative and thus the contribution of this term is to introduce a mean wall-normal force directed towards the wall. At locations other than channel centre, wall-normal velocity fluctuation is asymmetrically distributed. In particular, at $Re_\tau = 178.12$ the wall-normal velocity is negatively skewed over the region $6 < y_+ < 30$. In this region, the wallward fluid motion is more intense and

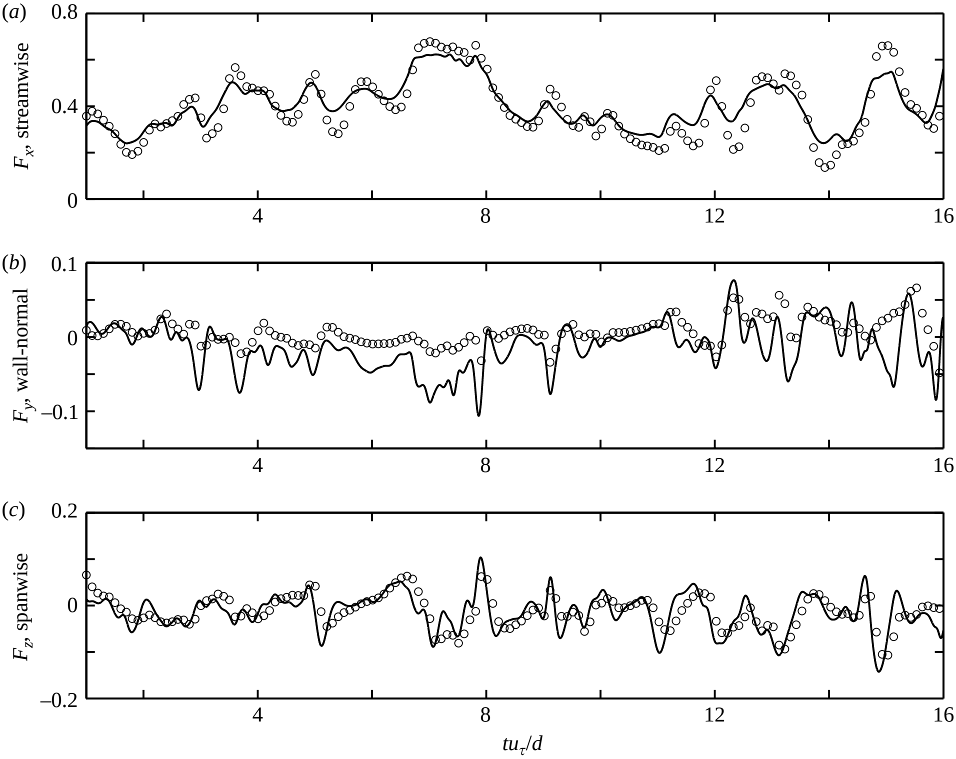

FIGURE 6. Same as figure 4 for $d_+ = 17.81$, $y_{p+} = 17.81$.

less frequent, while the outward ejection of near-wall fluid is less intense, but more frequent (Kim *et al.* 1987). The physical origin of this asymmetry can be traced to differences between the near-wall burst and sweep events. As a result of this asymmetry at $y_+ = 17.81$, the wall-normal velocity skewness (or $\langle u'^3_{y+}\rangle$) is negative and the third term in (3.14) also contributes negatively to wall-normal force.

The non-dimensional mean flow velocity varies from zero at the wall to a maximum of about 18 at the channel centreline and is about 11.8 at $y_+ = 17.81$ (see figure 2). At this location, the value of Reynolds stress is $\langle u'_{x+}u'_{y+}\rangle \approx -0.63$ and $\langle u'^3_{y+}\rangle \approx -0.22$. Thus it can be seen that the contribution from Reynolds stress to wall-normal force is the largest. For the largest two particles, $d_+ = 17.81$ and 24.94, (3.14) yields wall normal forces of -1.1×10^{-3} and -1.9×10^{-3}, respectively. The computed wall-normal forces (see table 2) are larger in magnitude and the difference is likely to be due to shear and wall-induced lift mechanisms, which will further be discussed in § 3.2.1.

The r.m.s. streamwise fluctuation proportionately increases with the mean streamwise force. The level of fluctuation in the wall-normal and spanwise forces is somewhat (about three times) weaker than those of the streamwise component, which agrees with the findings of Bagchi & Balachandar (2003) for the case of isotropic turbulence. In contrast, Merle *et al.* (2005) observed the wall-normal fluctuation to be more than an order of magnitude larger than the streamwise force fluctuation. They attributed the difference to the importance of the inertial contribution to lift force in the case of a bubble, whereas for a rigid particle at higher Reynolds number, the contribution from lift is typically quite small.

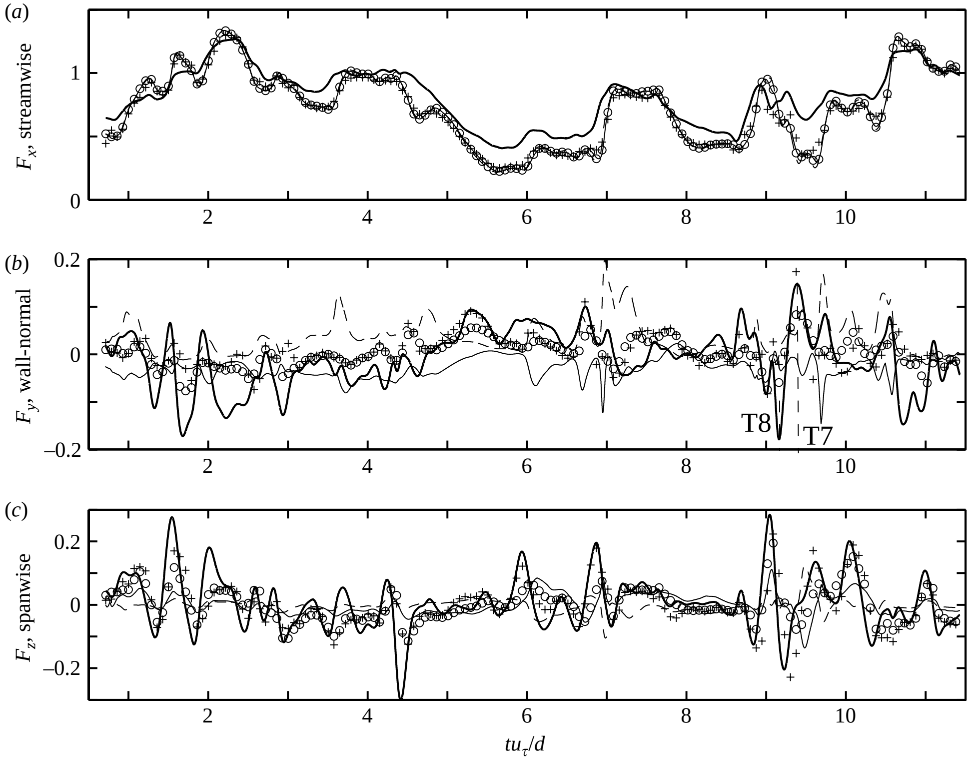

FIGURE 7. Same as figure 4 for $d_+ = 24.94$, $y_{p+} = 17.81$. In addition to DNS and standard drag predictions, enhanced predictions are included. +, standard drag plus added-mass contribution (scaled down by factor 6); — — —, standard drag plus Mei's lift formulation; thin sold line, Standard drag plus Kurose & Komori's lift correlation (scaled down by factor 3).

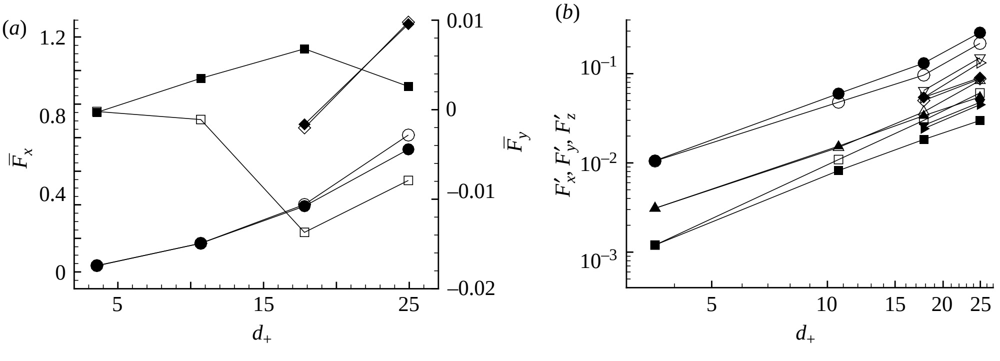

FIGURE 8. (*a*) Mean and (*b*) r.m.s. force components for the six different cases considered. Open symbols are the DNS result and the filled symbols are predictions from standard drag. ○, streamwise component; □, wall-normal component; △, spanwise component are for particles placed in the buffer region. ◇, streamwise component; ▽, wall-normal component; ▷, spanwise component are for particles placed in the channel centre.

The instantaneous ups and downs of the force components are well predicted only for the smallest particle under consideration. With increasing particle size, the actual force fluctuation increasingly departs from the prediction based on standard drag correlation. In the case of streamwise force, the departure is primarily in the high-frequency component. Even for the largest particle under consideration ($d_+ = 24.94$), the low-frequency variation appears to be in response to changes in the streamwise component of the ambient flow, as indicated by the close correspondence between the actual force and the standard drag prediction in terms of their slow variation. For the larger particles, the overall level of fluctuation, as measured by r.m.s., computed in the DNS is lower than that predicted based on standard drag correlation. Quantitatively, the standard drag correlation tends to over-predict streamwise force fluctuation by about 30 %. Alternative definitions of $\boldsymbol{u}_+$ based on local volume or time average reduces the level of fluctuation, but do not yield an improved prediction of the instantaneous force. Thus, the cause of reduced streamwise force fluctuation experienced by the particle lies elsewhere.

In contrast to streamwise force, the level of fluctuation in the computed wall-normal force far exceeds prediction based on standard drag correlation. For example, for the largest particle investigated ($d_+ = 24.94$) the wall-normal force fluctuation is 100 % larger than that predicted. In the case of streamwise force, the difference was primarily in amplitude, while the frequency of fluctuation was reasonably well captured by the standard drag correlation. In the case of wall-normal force, a substantial difference exists both in the amplitude and frequency of fluctuation. The increased level of fluctuation and the appearance of a high-frequency component suggest the possible influence of vortex shedding in the wake of the particle. The effect of wake vortex shedding and the role of associated lift force contributing to the wall-normal force will be investigated below.

3.2. *Pressure gradient, added mass and lift contributions*

Here we estimate the pressure gradient and added-mass forces on the particle and evaluate their importance to force estimation. Note that in the present context, the particle is held fixed and hence particle acceleration is identically zero. Thus, the pressure gradient, and added-mass forces arise only from fluid acceleration seen by the particle. An enhanced force prediction that includes these additional contributions can be expressed as

$$\boldsymbol{F}_{en} = \boldsymbol{F}_{std} + \boldsymbol{F}_{am}, \tag{3.15}$$

where the pressure gradient and the added-mass forces have been combined since they have the same form. The standard drag contribution, $\boldsymbol{F}_{std}$, is the same as given in (3.2). The added-mass plus pressure gradient contribution can be written in non-dimensional form as

$$\boldsymbol{F}_{am} = \frac{\pi}{4}\left(\frac{d_+}{Re_\tau}\right)^3 \frac{\mathrm{D}\boldsymbol{u}_+}{\mathrm{D}t_+}. \tag{3.16}$$

The added-mass force depends only on the instantaneous total acceleration of the flow, $\mathrm{D}\boldsymbol{u}_+/\mathrm{D}t_+$, at the location occupied by the particle. This quantity must also be evaluated under undisturbed conditions, and we obtain this in a manner similar to the undisturbed fluid velocity at the particle location. Note that the conventional scaling that the added-mass force is proportional to fluid-to-particle density ratio applies only to the added-mass force arising from particle acceleration. The added-mass contribution arising from fluid acceleration is independent of density ratio, and in a channel flow it scales as $(d_+/Re)^3 = (d/H)^3$ (also see Bagchi & Balachandar 2003). Pan & Banerjee (1996, 1997) have considered force on a freely moving particle in a turbulent channel flow in the frequency domain and argued that for $d_+ < O(1)$, the contribution from added-mass and Basset history are much smaller than the quasi-steady drag force. The added-mass contribution can thus be expected to be negligible for the smallest particle under consideration, and this has been confirmed by computation. In figure 7, for the largest particle under consideration, the time history of the different force components predicted with the inclusion of the pressure gradient and added-mass contributions are plotted.

The computed added-mass force follows the analytic scaling and even for the largest particle, the added-mass force is substantially lower than the standard drag contribution. In the streamwise component, the inclusion of the added-mass contribution makes only a small difference. In the wall-normal and spanwise components, the inclusion of the added-mass contribution makes an appreciable difference. In the streamwise component, the added-mass contribution when added to the standard drag, lowers both the predicted mean and the level of fluctuation. The mean streamwise force predicted by the standard drag model was consistently lower than that measured in the DNS and with the inclusion of the added-mass contribution this departure increases in magnitude. Whereas, the lower r.m.s. streamwise force fluctuation improves agreement with the DNS result, although the predicted r.m.s. is still substantially larger than that measured in the DNS. The effect of the added-mass contribution on wall-normal force is similar. With its inclusion, the difference between the predicted and the actual DNS mean wall-normal force increases. On the other hand, with the inclusion of the added-mass contribution, the predicted r.m.s. fluctuation in wall-normal force increases and quantitatively approaches the level of fluctuation computed from the DNS. Despite such quantitative improvement, from figure 7 it is clear that the inclusion of the added-mass contribution does not improve the predictive capability of the instantaneous force on the particle.

The Basset history force on the particle can be computed as

$$\boldsymbol{F}_{bh} = \frac{3\pi d_+}{Re_\tau^2} \int_{-\infty}^{t_+} k(t_+, \tau_+) \frac{\mathrm{D}\boldsymbol{u}_+}{\mathrm{D}\tau_+}\, \mathrm{d}\tau_+, \tag{3.17}$$

and included in the enhanced force prediction in (3.15). However, the appropriateness of the history contribution in the present case of a stationary particle can be questioned. In a freely moving particle, the history force arises from the integration of past relative acceleration between the particle and the surrounding fluid weighted by the kernel, $k(t_+, \tau_+)$. In the case of a stationary particle, (3.17) simply reduces to weighted time integration of local fluid acceleration. The long-time integral of local fluid acceleration is simply zero. For large particles, whose time scale is larger than the time scale on which fluid acceleration varies, the effect of the weighting kernel is negligible. Thus, the inclusion of Basset history force is more appropriate for the case of a moving particle. Nevertheless, in all the cases considered, we have computed the history contribution with (3.17), using the kernel given by Mei & Adrian (1992), and the contribution is quite small (not shown here).

3.2.1. *Lift force*

In this section, we examine the adequacy of existing shear-induced lift correlations for their ability to capture the enhanced fluctuation observed in the computed wall-normal force. We define an enhanced model for force on the particle to include both the standard drag contribution and a shear-induced lift contribution as shown below

$$\boldsymbol{F}_{en} = \boldsymbol{F}_{std} + \boldsymbol{F}_L. \tag{3.18}$$

The lift force will be parameterized in terms of local vorticity ($\boldsymbol{\Omega}_+$) and relative velocity ($\boldsymbol{u}_+$) as follows

$$\boldsymbol{F}_L = C_L \frac{\pi}{6}\left(\frac{d_+}{Re_\tau}\right)^3 \boldsymbol{u}_+ \times \boldsymbol{\Omega}_+, \tag{3.19}$$

where C_L is the lift coefficient and different theoretical models and empirical correlations for C_L have been proposed in the past. Their effectiveness in capturing the computed force on the particle will be investigated.

Using inviscid analysis, Auton (1987) obtained an analytic expression for lift force on a spherical particle in terms of the local vorticity of the ambient flow. In the case of a clean bubble placed at the centre of a turbulent pipe flow, Merle *et al.* (2005) observed that Auton's lift provided a good model for the actual lift force experienced by the bubble. In the present case of a rigid non-slip particle, substantial vorticity is generated at the particle surface, which results in significant reduction in the lift force and perhaps even a reversal in direction (Kurose & Komori 1999; Bagchi & Balachandar 2002*b*). Thus, Auton's formulation can be expected to overpredict significantly the lift force observed in the present simulations.

The classic analysis for shear-induced lift by Saffman (1965) (also see Moore & Saffman 1968) is applicable in the limit $Re \ll 1$, $Re_G = Gd^2/\nu \ll 1$ and $\sqrt{Re_G}/Re \gg 1$, where G is the shear magnitude of the ambient flow. McLaughlin (1991) extended Saffman's theory and relaxed the requirement of $\sqrt{Re_G}/Re \gg 1$. From the results given in Saffman (1965), Dandy & Dwyer (1990) and McLaughlin (1991), Mei (1992) developed an approximate lift expression that is applicable for small Reynolds numbers. Based on their numerical simulations, Kurose & Komori (1999) have obtained an empirical expression for lift force that is applicable for a wider range of Re.

Here we will test the above four models of lift force (Auton's inviscid lift, Saffman's low Re shear-lift, Mei's improvement, and Kurose & Komori's finite Re empirical correlation). All these models have been developed for the canonical case of a rigid particle subjected to an unbounded linear shear flow; but we apply them in the context of a wall-bounded turbulent flow and therefore we must exercise caution in the interpretation of the results. In a turbulent flow, it is not possible to define unambiguously local linear shear and as a result the lift models have been re-cast in terms of local relative velocity and local ambient flow vorticity, both of which can be defined well. Rewriting the lift forces of Auton, Saffman and Mei in the form expressed in (3.1), the corresponding lift coefficient C_L can be expressed as

$$C_L = \begin{cases} 1/2 & \text{Auton's}, \\ \dfrac{12.92}{\pi}\dfrac{\sqrt{Re_\Omega}}{Re} & \text{Saffman's}, \\ 0.0524 C_{L,Saffman}(\alpha Re)^{1/2} & \text{Mei's}, \end{cases} \tag{3.20}$$

where $Re_\Omega = \Omega d^2/\nu$ is the local vorticity-based Reynolds number, and $\alpha = \Omega d/2|\boldsymbol{u}|$. Kurose & Komori's empirical correlation is treated similarly.

In the above formulation, the lift force is dictated to be orthogonal to both the undisturbed fluid velocity and the undisturbed fluid vorticity at the location occupied by the particle. Since fluid velocity and vorticity are preferentially directed along streamwise and spanwise directions, the predicted lift force is predominantly directed towards the channel centre. The presence of high- and low-speed streaks in the wall region contributes to the spanwise shear of the streamwise velocity, which gives rise to a spanwise directed lift component. As will be seen below, the strongest impact of the lift is in the wall-normal force and then in the spanwise force. The effect of lift on the streamwise component of force is more than an order of magnitude weaker.

The force components are shown in figure 7 for the largest particle ($d_+ = 24.94$) with the inclusion of the lift force. In the figure, only the results with the inclusion of Mei's correction and Kurose & Komori's correlation are shown, as the other two lift models are observed to perform worse in the present case. The mean and r.m.s. statistics for all four particle sizes are shown in table 2. From (3.19), it is clear that the scaling of shear-induced lift is similar to that of added-mass force. However, note that the value of the lift coefficient (C_L) is widely varying between the different estimates, thus, resulting in orders of magnitude differences in the predicted lift force. For the smallest particle, the different lift force estimates make little contribution to the overall force (see table 2). With increasing particle size, the impact of including lift in force estimation becomes substantial.

Typically, the inviscid lift by Auton is quite large for the larger particles. As can be expected, the lift force on a rigid sphere does not follow the inviscid prediction. Furthermore, Saffman's lift formula is used outside its range of validity, since the condition $\sqrt{Re_G}/Re \gg 1$ is not typically satisfied in the present case. It can be observed that Saffman's formula also tends to over-predict the lift force on the particle, but not as much as Auton's inviscid prediction. Based on results from finite-Reynolds-number simulations in unbounded shear (Kurose & Komori 1999; Bagchi & Balachandar 2002*a*), the shear-induced lift force is expected to be much weaker than Saffman's prediction at the particle Reynolds numbers under consideration.

The mean wall-normal force predicted from the standard drag model and with the inclusion of the lift force, as given in Auton, Saffman and Mei's estimates, remains positive, indicating a force component directed towards the channel centre. The actual wall-normal component of force on the particle as measured in the DNS is consistently negative. In other words, the actual hydrodynamic force on the particle tends to push it towards the wall. Except for the smallest particle, the Reynolds number based on particle diameter and relative velocity is in excess of 100, and at such Reynolds numbers Kurose & Komori (1999) and Bagchi & Balachandar (2002*a*) observed negative lift on a rigid spherical particle in unbounded linear shear flow. The relatively small magnitude of the mean wall-normal force and its direction towards the wall measured in the present simulations are statistically consistent with that predicted with Kurose & Komori's correlation. Furthermore, the level of wall-normal force fluctuation is also reasonably well estimated by Kurose & Komori's correlation. However, figure 7 shows that none of the deterministic predictive formula is able to reproduce the actual force history. In the present context, the shear flow around the particle is not unbounded and the effect of channel walls must be addressed as well.

3.3. *Particle at channel centre*

Here we discuss the final two cases shown in table 1, where the particle is placed at the centre of the channel and thus the effect of the channel wall is at its minimum. These simulations are similar to those for an isolated stationary clean bubble placed along the centreline of a turbulent pipe flow considered by Merle *et al.* (2005). The bubble Reynolds number in their simulation was 500 and the bubble diameter was 8.3 times the Kolmogorov scale. The present results can also be compared with those of Bagchi & Balachandar (2003), who considered the interaction of a particle with isotropic free-stream turbulence. The particle Reynolds number and the ratio of particle to Kolmogorov scale considered by Bagchi & Balachandar (2003) are comparable to the

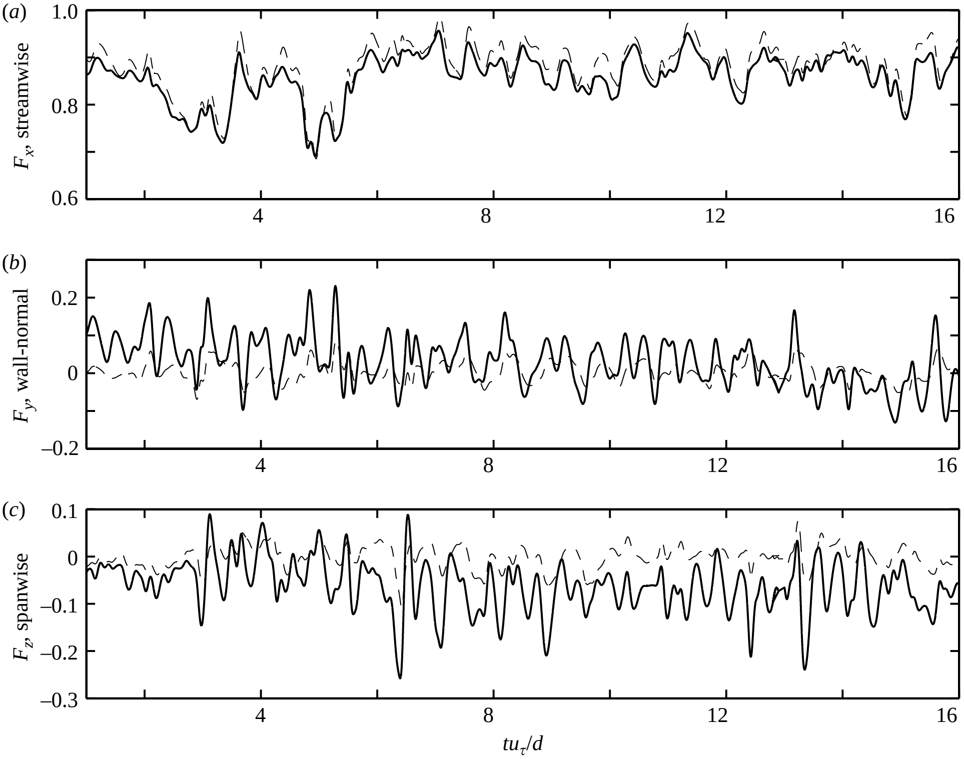

FIGURE 9. Time history of the force components for $d_+ = 17.81$, $y_{p+} = 178.1$. (*a*) Streamwise force; (*b*) wall-normal force; (*c*) spanwise force. ——, present DNS results; - - -, forces predicted using the standard drag formulation.

present cases. However, in the present case of turbulent channel flow at $Re_\tau = 178.1$, the r.m.s. fluctuation at the channel centre is only 4.09 % of the mean centreline velocity, which is considerably lower than those investigated by Merle *et al.* (2005) and Bagchi & Balachandar (2003). Thus the present simulations of particles at the channel centre correspond to the limit of weak turbulence compared to mean relative velocity.

Figures 9 and 10 show the time history of the computed DNS streamwise, wall-normal and spanwise forces for $d_+ = 17.81$ and 24.94 placed at the channel centre. Also plotted in the figures are the corresponding predictions based on standard drag law. The statistical information on the r.m.s. lift force is presented in table 1. In both these cases, the streamwise force is extracted well by the standard drag correlation. The contribution from added-mass is small and tends to lower the level of predicted fluctuation and improve the quantitative comparison with the DNS value. Similar good agreement was observed for the streamwise force by Merle *et al.* (2005), however, for their case of a clean spherical bubble, the standard drag law given in (3.2) must be replaced by the expression by Moore (1963).

In the case of a rigid particle subject to free-stream isotropic turbulence, Bagchi & Balachandar (2003) observed standard drag prediction to be reasonably accurate only for their smallest particle. Owing to the higher level of free-stream fluctuation velocity in their simulations (10 % to 25 %), with increasing particle size they observed the computed DNS force on the particle to depart substantially from the standard

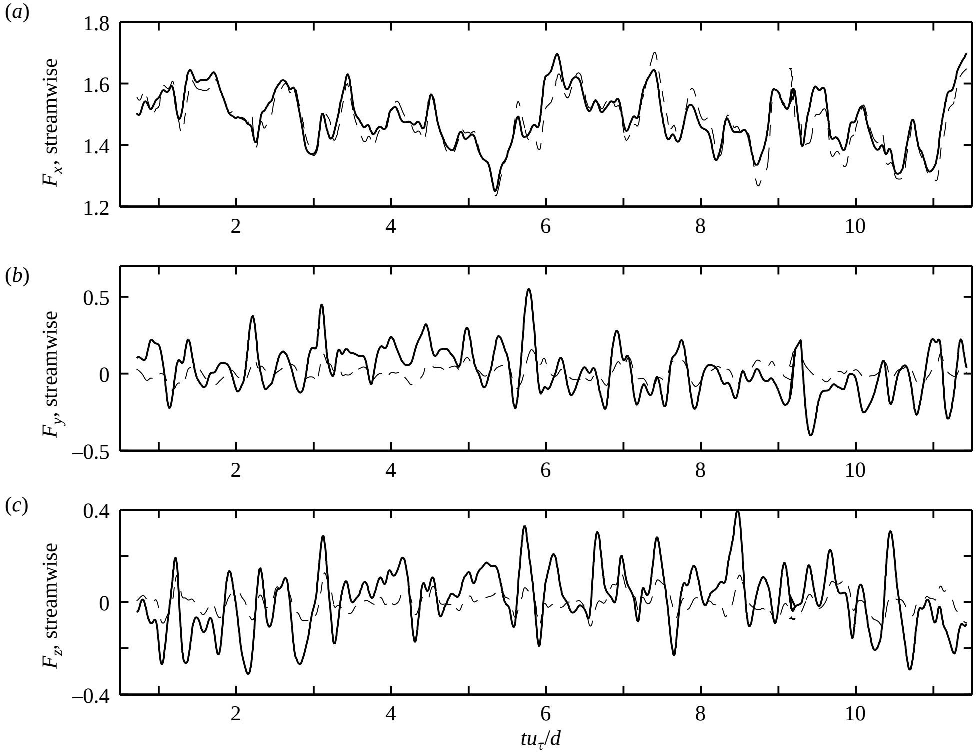

FIGURE 10. Same as figure 9 for $d_+ = 24.94$, $y_{p+} = 178.1$.

drag prediction. The deviation from the standard drag prediction was due to strong vortex shedding and significantly enhanced turbulence fluctuation generated in the particle wake (Bagchi & Balachandar 2004). By fixing the particle position, here we have constrained the r.m.s. ambient flow velocity fluctuation to be about 4 % of the mean relative velocity. If we allow the particle to move with the fluid, the relative fluid velocity seen by the particle would decrease. As a result, on one hand, the r.m.s. fluctuation to mean fluid velocity seen by the particle will increase; on the other hand the particle Reynolds number based on relative velocity will decrease. Thus for a large particle in free motion in a turbulent channel, a complete answer to how well the standard drag can predict the streamwise force requires further investigation.

In contrast to the streamwise component, the standard drag does not accurately capture the instantaneous wall-normal and spanwise components. The inclusion of added-mass contribution does not help in the prediction either. Compared to a particle of the same size placed in the buffer region, a particle along the channel centre results in substantially enhanced fluctuation in the wall-normal and spanwise components (F_y' more than doubles at the channel centre). The r.m.s. fluctuation in the streamwise component is, however, substantially reduced at the channel centre. The reduction in r.m.s. streamwise component from the buffer region to the channel centre is understandable, since the ratio of r.m.s. fluctuation to mean fluid velocity decreases from 23.16 % at $y_{p+} = 17.81$ to 4.09 % at $y_{p+} = 178.1$. In comparison, the 50 % reduction in r.m.s. streamwise force appears modest. The mean particle Reynolds numbers for the two cases (see table 1) are clearly well above the critical value and can support strong vortex shedding even in the absence of any ambient turbulence.

Thus, the increase in wall-normal and spanwise force fluctuation is due to enhanced vortex shedding. Such force fluctuation resulting from the stochastic natural shedding of vortices cannot be accounted for with any of the deterministic lift force formula that are based on ambient shear (or vorticity).

4. Discussion

For a particle subjected to turbulent crossflow, there are two sources that contribute to temporal fluctuation in the force it experiences. The first arises from the time variation of the ambient turbulent flow seen by the particle. In the context of wall turbulence, the passage of low- and high-speed streaks over the particle can be expected to yield streamwise force fluctuation. The occurrence of turbulent ejection and sweep events close to the particle will contribute to wall-normal force fluctuation and similarly the presence of quasi-streamwise vortices close to the particle can yield a fluctuating spanwise force on the particle. The second source of force fluctuation arises from the natural chaotic shedding of vortices in the wake of the particle.

In the first mechanism, any fluctuation in the particle force is fully correlated with the ambient flow and thus can be deterministically expressed in terms of the relative velocity between the particle and the ambient flow. In contrast, fluctuation arising from vortex shedding is self-induced and is fundamentally stochastic in nature. The vortex-shedding process may be induced and somewhat influenced by ambient turbulence, but it is not fully correlated with the ambient flow seen by the particle. The smallest ($d_+ = 3.56$) particle placed at $y_+ = 17.81$ provides a convenient case to study the deterministic component in isolation, since in this case the particle Reynolds number is low and there is no stochastic contribution arising from vortex shedding; whereas the largest particle placed in the buffer layer, as well as the two cases of particle in the centre of the channel, are the most influenced by vortex shedding.

4.1. *Turbulent flow structures and force fluctuation*

A detailed probing of the incoming turbulent flow structures as they pass over the particle was conducted for all the particles. However, as seen in figure 4, the force on the smallest particle ($d_+ = 3.56$ at $y_+ = 17.81$) shows very good correlation with the ambient turbulent flow and therefore this case will be analysed in greater detail.

Figure 11 shows contours of streamwise fluid velocity on a horizontal (x, z)-plane ($y_+ = 5$) at two different time instances, which are marked as T1 and T2 in figure 4(*a*). Figure 11(*a*) corresponds to an instance of enhanced drag and figure 11(*b*) corresponds to an instance of low drag. Black indicates lower streamwise velocity and the white corresponds to higher streamwise velocity. The high- and low-speed turbulent streaks are evident at both time instances. In figure 11(*a*), the particle is located in a high-speed streak, and at the later time shown in figure 11(*b*) a low-speed streak has moved over the particle. The streamwise force fluctuation for the small particle located close to the wall can be fully correlated with the time-dependent motion of the high- and low-speed streaks. Similar investigation shows that even for the largest particle under consideration, the lower-frequency fluctuations seen for the streamwise force in figure 7 are due to the passage of high- and low-speed streaks. As a result, such fluctuations can be reasonably well predicted with a knowledge of the time-dependent ambient flow. Note that a freely moving particle may not explore the high- and low-speed streaks with equal probability. Pan & Banerjee (1996) show that particles smaller than or equal in size to the Kolmogorov scale are nearly uniformly distributed and thus can be taken to equally explore the high- and low-speed streaks in the near-wall region.

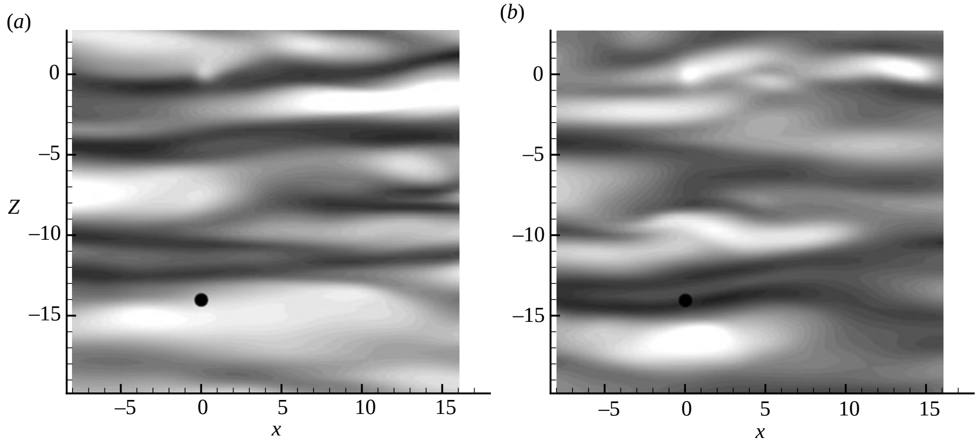

FIGURE 11. Contours of streamwise velocity on the (x, z)-plane passing through the particle for $d_+ = 3.56, y_{p+} = 17.81$ at (a) $tu_\tau/d = 14.20$ highlighting a high-speed streak and (b) $tu_\tau/d = 42.17$ highlighting a low-speed streak.

On the other hand, Pan & Banerjee (1996) observed larger particles to congregate in regions of low-speed streak, thus potentially increasing the probability of lower streamwise force.

The strong wallward (negative) y-force is connected with a rapid inrush of fluid towards the wall during a sweep event. Correspondingly, ejection events, where fluid is pumped away from the wall, as they pass over the particle, contribute to a strong positive wall-normal force. Examples of such events are depicted in figures 12(a) and 12(b), where contours of perturbation spanwise vorticity are plotted on an (x, y)-plane passing through the centre of the particle, for the smallest particle case. Here the mean spanwise vorticity arising from the mean flow has been subtracted and the light and dark shades, respectively, correspond to clockwise and anticlockwise vorticity. Figure 12(a) is at $tu_\tau/d = 41.00$ and corresponds to an instance of peak positive lift force and figure 12(b) is at $tu_\tau/d = 15.30$ when the wall-normal force is at a negative peak (these times are marked in figure 4(b) as T3 and T4).

A close investigation of the flow field at $tu_\tau/d = 41.00$ shows the presence of a hairpin packet located near the particle. The individual hairpin vortices are characterized by compact regions of intense clockwise rotation in figure 12(a) (marked E1 to E5). The occurrence of such packets of hairpin-like vortices in wall-turbulence has been well documented (Zhou *et al.* 1999 Christensen & Adrian 2001). As seen in the figure, the hairpin-like vortices line up along the streamwise direction and their cooperative action results in an ejection event of strong quadrant-2 activity, i.e. pumping of fluid away from the wall ($v' > 0$) and backwards ($u' < 0$). In particular, the vortices marked E3, E4 and E5, which are closer to the particle, play the strongest role in the ejection event seen by the particle.

The hairpin packet itself is a stable structure and is relatively long lived; but as seen by a fixed probe, its passage is quite rapid, and registered as an intense quadrant-2 ejection event. In the present case of a stationary particle, the corresponding increase in wall-normal force is intense and short lived. The occurrence of such a strong positive lift force was also registered in the instantaneous force measurement on particles sitting on the wall in a turbulent boundary layer (Mollinger & Nieuwstadt 1996). Thus, the ejection events can be conjectured to be one of the primary mechanisms for intense

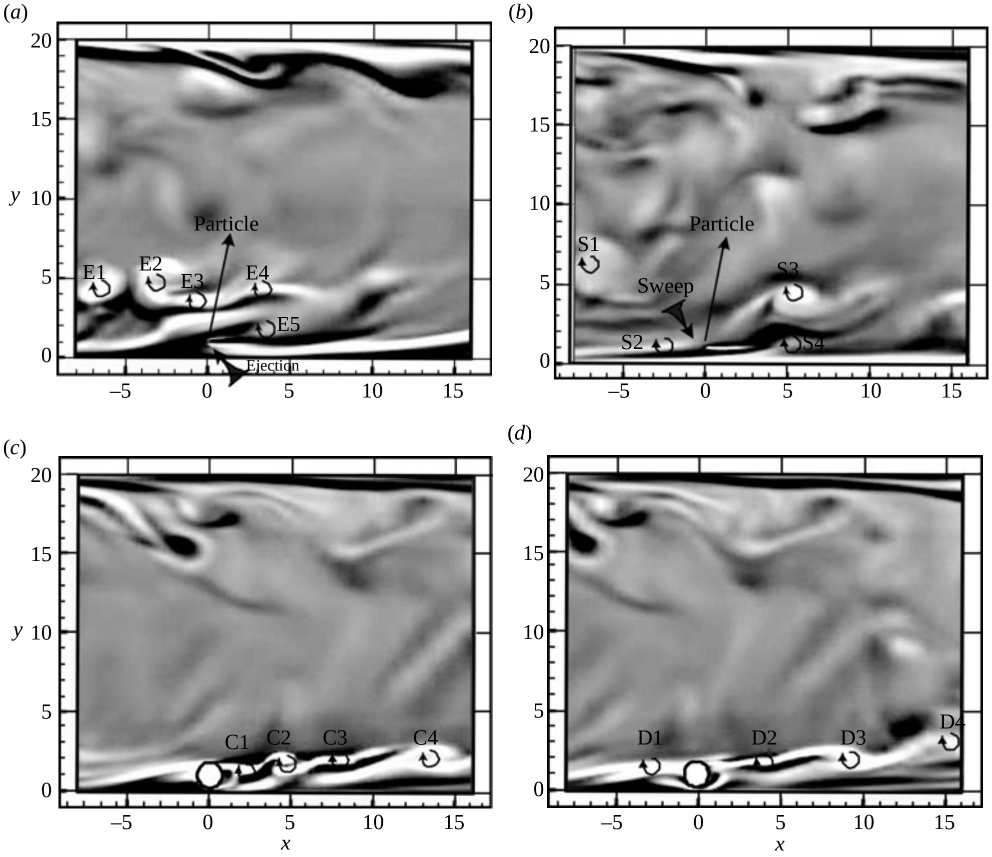

FIGURE 12. Contours of spanwise vorticity on the (x, y)-plane passing through the particle. (*a*) and (*b*) are for the smallest particle ($d_+ = 3.56, y_{p+} = 17.81$) at $tu_\tau/d = 14.20$ and $tu_\tau/d = 42.17$, respectively. These instances are marked in figure 4(*b*). The compact intense regions of clockwise vorticity are indicative of hairpin vortices and are marked in the figures. (*c*) and (*d*) are for the largest particle ($d_+ = 24.94, y_{p+} = 17.81$) at $tu_\tau/d = 9.39$ and $tu_\tau/d = 9.16$, respectively. These instances are marked in figure 7(*b*). In these later frames the compact intense regions of clockwise vorticity are indicative of shed vortices and are marked as well.

wall-normal force and consequently they contribute strongly to the resuspension of particles from a bed into the flow. It is of interest to investigate the effect of such ejection events on particles which are already suspended and moving with the flow. On one hand, as the particle moves with the flow, its exposure to an ejection event will be longer lived. This is unlike a stationary particle, which sees only the ejection for a brief period as the event rapidly passes by. On the other hand, for a particle moving with the flow, the relative velocity between the particle and the flow decreases, thus altering the drag and lift forces on the particle.

Figure 12(*b*) shows an instance of strong wallward flow over the particle. Signatures of hairpin vortices can be observed as S1 and S3, but they are sufficiently farther away from the particle to have a strong influence. An incipient vortex marked S2 is located close to the wall, upstream of the particle, and it perhaps has the strongest effect on the particle. A broad inrush of fluid towards the wall contributes to the strong negative wallward force on the particle. Each and every one of the strong lift

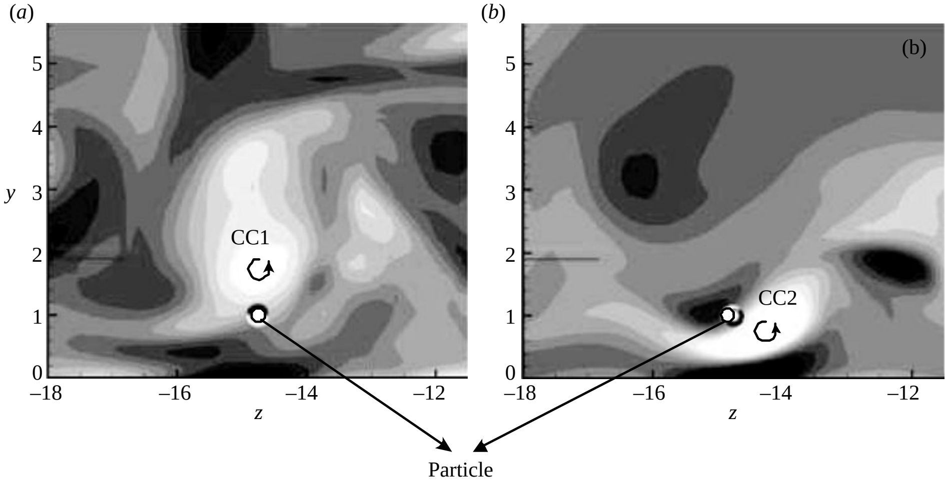

FIGURE 13. Contours of streamwise vorticity on the (z, y)-plane passing through the particle for the smallest particle ($d_+ = 3.56$, $y_{p+} = 17.81$). (*a*) $tu_\tau/d = 39.40$; (*b*) $tu_\tau/d = 15.35$. These instances are marked in figure 4(*c*). The compact intense regions of clockwise vorticity are indicative of quasi-streamwise vortices.

peaks and valleys can similarly be correlated with an ejection or sweep event. The interaction of finite-sized particles with ejection and sweep events has been considered in the pioneering work of Pan & Banerjee (1996), who showed the corresponding back influence of such interaction on the statistics of wall turbulence.

Fluctuation in the spanwise component of the force for the smallest particle can also be correlated with the turbulent structures of the flow. As can be expected, the dominant effect on the spanwise force comes from the quasi-streamwise vortices. Figure 13 shows contours of streamwise component of vorticity on the (z, y)-plane in the neighbourhood of the particle at two different instances when the spanwise force is at an extreme. These instances are marked T5 and T6 in figure 4(*c*). In figure 13(*a*) a strong counterclockwise vortex (marked CC1) is located just above the particle and its induced velocity contributes to a strong force direct to the right of the particle. The instance shown in frame (*b*) is also marked by the presence of a counter-clockwise vortex (CC2), which is located to the lower right of the particle. The resulting induced flow contributes to a strong leftward-directed spanwise force on the particle.

Regions of compact intense streamwise vorticity in wall turbulence can be due to either the legs of the hairpin or cane-like vortices or the quasi-streamwise vortices, which are often observed without any discernible head associated with them (Brooke & Hanratty 1993). These quasi-streamwise vortices are of both signs (clockwise and counterclockwise rotating on the (z, y)-plane) and when they are located close to the particle, depending on their sense of rotation and location, have a strong influence on the spanwise force on the particle. As discussed above, the hairpin vortices and their quasi-streamwise legs also have a strong influence on the wall-normal force. All of the spanwise force extrema observed in figure 4(*c*) can similarly be correlated with the presence of a quasi-streamwise vortex in the neighbourhood of the particle. At other instances, the quasi-streamwise vortices, although still present, are sufficiently farther away from the particle to have a strong effect.

4.2. *Vortex shedding*

As the particle size increases, its interaction with the incoming turbulent flow structures can be expected to be complex. This interaction is further complicated by the particle starting shed to vortical structures of its own. An isolated particle subject to uniform crossflow, at sufficiently large Reynolds numbers, shows strong fluctuation in lift force resulting from periodic vortex shedding (Bagchi, Ha & Balachandar 2001). The corresponding fluctuation in the drag force is observed to be significantly weaker. In an unbounded uniform ambient crossflow-the wake behind a spherical particle becomes unsteady for $Re > 270$ and a periodic train of one-side vortices are shed (Natarajan & Acrivos 1993; Johnson & Patel 1999). With increasing Reynolds number, the shedding process becomes chaotic and as a result the lift force on the particle exhibits large quasi-periodic fluctuation (Tomboulides & Orszag 2000; Bagchi *et al.* 2001). As shown in table 1, the Reynolds numbers for cases 3 to 6 are sufficiently high and the large fluctuation observed in the computed wall-normal force component for these cases is due to vortex shedding.

In the present context, the onset of unsteadiness and chaotic vortex shedding are influenced by ambient turbulence and also by the presence of the channel walls. The effect of turbulence is to promote early onset of chaotic vortex shedding and also to strengthen the shedding process (Mittal 2000; Bagchi & Balachandar 2004). The effect of the nearby wall is more subtle. The additional asymmetry introduced by the wall promotes early onset, whereas the wall-induced viscous effect is likely to delay the onset of chaotic shedding. For the case of a spherical particle falling parallel to a vertical wall in a quiescent fluid, it was observed that for a particle very close to the wall, viscous effect dominates and the onset of vortex shedding is delayed. However, for a particle sufficiently far away from the wall, the asymmetric effect promotes an early onset (Zeng *et al.* 2005). Based on these factors, we can expect vortex shedding to be present and to strongly influence the wall-normal force, provided the particle Reynolds number is of the order of 200 or more.

Note that the particle Reynolds number in table 1 is based on the mean relative velocity and therefore it is a time-averaged value. The streamwise velocity around the particle fluctuates over time, and as a result, the instantaneous particle Reynolds number can reach values much larger than the mean. Consistent with the above argument, we observe the wall-normal force on the smallest particle to follow the standard drag prediction and not exhibit any additional fluctuation. For the intermediate particle of $d_+ = 10.69$, over periods of time the wall-normal force is predicted well by the standard drag, but occasionally large fluctuation and departure from standard drag can be observed. The large fluctuation in the wall-normal force occurs precisely during periods of enhanced streamwise force. This suggests that during periods of strong streamwise flow, the instantaneous particle Reynolds number increases above a threshold to trigger episodes of vortex shedding. For the larger two particles, the Reynolds number is sufficiently large and therefore vortex shedding appears to be present over most of the time. The computed DNS wall-normal force thus exhibits large-amplitude fluctuation for most of the duration of the simulation.

Figures 12(*c*) and 12(*d*) show contours of perturbation spanwise vorticity on the (x, y)-plane passing through the particle, for the largest particle located in the buffer region ($d_+ = 24.94$, $y_{p+} = 17.81$). The two frames show two different time instances corresponding to a peak and valley in the lift force and these times are marked T7 and T8 in figure 7. At both these times a sequence of vortices can be seen in the wake of the particle. The vortex-shedding process appears to be one-sided and the effect

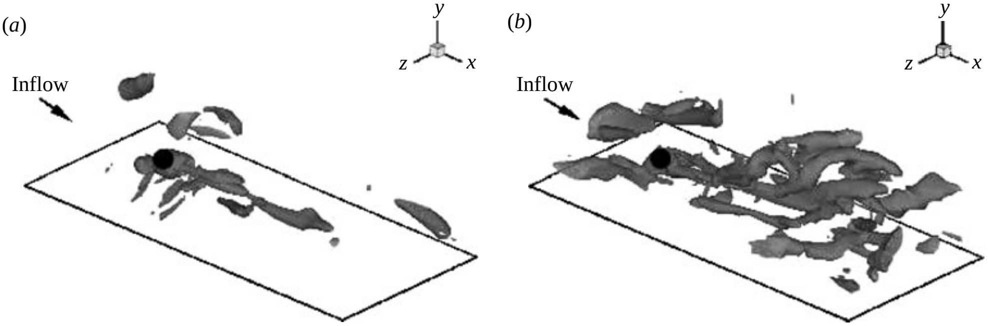

FIGURE 14. Iso-surface of swirling strength $\lambda_{ci} = 2.5$ for $d_+ = 17.81$, $y_{p+} = 17.81$ at (a) $tu_\tau/d = 0.025$ and (b) $tu_\tau/d = 2.5$.

of the bottom wall is to suppress the shedding of distinct vortices below the particle. At the time shown in figure 12(c), the vortex marked C1 has just formed and is in the process of being shed. The resulting low pressure above the particle contributes to the strong positive lift force experienced by the particle. In contrast, at the time shown in figure 12(d), the shed vortices are farther downstream of the particle, but a vortex marked D1 can be seen to approach the particle from upstream. This vortex is not shed from the sphere, but is part of wall turbulence.

Based on detailed views of the instantaneous three-dimensional flow field, we observe that the wake-shedding process is not strongly correlated with the incoming turbulent vortical structures. The only exception is for the intermediate particle size, where vortex shedding is episodically observed when the ambient flow velocity increases above a threshold. Figure 14 shows a three-dimensional view of the incoming turbulent and shed vortical structures at two different time instances ($tu_\tau/d = 0.025$ and $tu_\tau/d = 2.5$) for the case $d_+ = 17.81$ at $y_{p+} = 17.81$. Plotted in this figure are iso-surfaces of swirling strength, which is defined as the imaginary part of the complex eigenvalue of the local velocity gradient tensor. Swirling strength has been established to extract coherent vortical structures in complex turbulent flows unambiguously (Zhou *et al.* 1999; Chakraborty, Balachandar & Adrian 2005). Animations showing the dynamics of these vortical structures are revealing. In particular, the strong fluctuation in the wall-normal and spanwise components of force for the larger particles can be correlated well with the wake vortex-shedding process.

The two-time correlation of wall-normal force defined as

$$corr(\tau) = \frac{\displaystyle\int_{t=0}^{T-\tau} F_y(t)F_y(t+\tau)\mathrm{d}t}{\displaystyle\int_{t=0}^{T-\tau} F_y(t)^2\mathrm{d}t}, \tag{4.1}$$

is shown in figure 15(a) for the largest particle in the buffer region. Here, T is the total duration of time integration and τ is non-dimensional time separation, non-dimensionalized by $\langle u^*(y_{p*})\rangle/d$, where $\langle u^*(y_{p*})\rangle$ is the averaged fluid velocity at the particle centre. Two peaks located at non-dimensional time periods of 4.93 and 9.11 can be observed. These peaks are somewhat broad and thus indicate some variation in the shedding period. The corresponding power spectra of the wall-normal force is shown in figure 15(b), where frequency is non-dimensionalized by $d/\langle u^*(y_{p*})\rangle$. Corresponding to the peaks in the two-time correlation, we observe enhanced energy around $St = 0.11$ and $St = 0.203$. From the spectra of the wall-normal force seen in

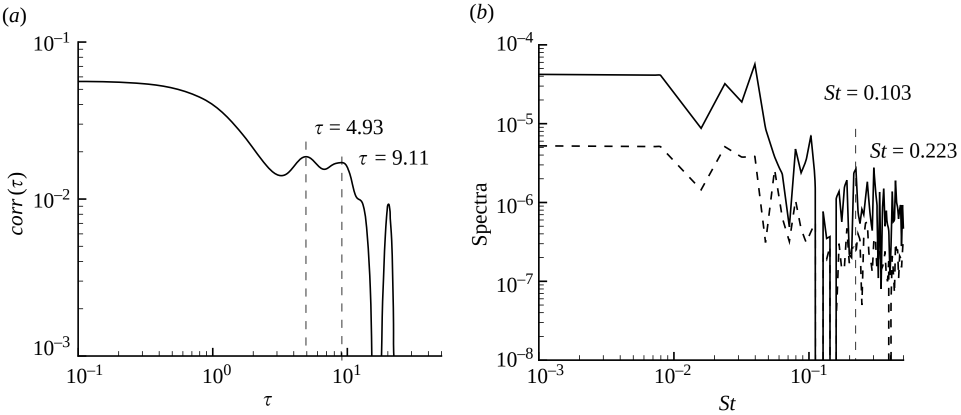

FIGURE 15. (*a*) Two-time correlation of wall-normal force and (*b*) spectra of wall-normal force for $d_+ = 24.94$, $y_{p+} = 17.81$. ——, DNS result; - - -, standard drag correlation.

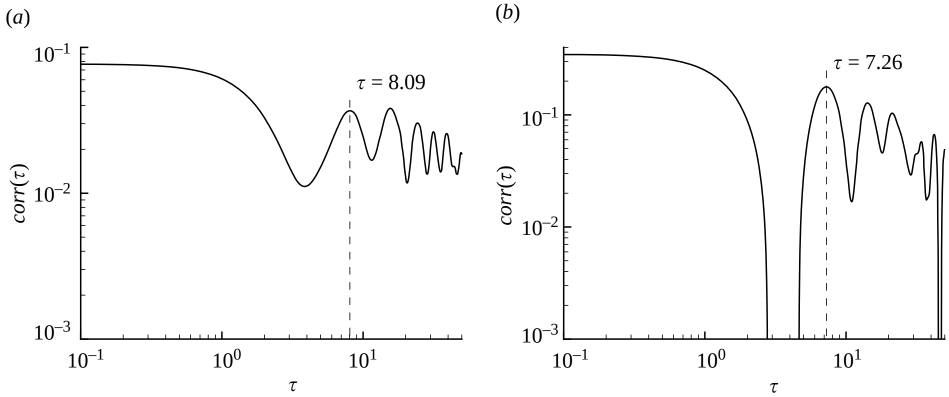

FIGURE 16. Two-time correlation of wall-normal force for $y_{p+} = 178.1$. (*a*) $d_+ = 17.81$; (*b*) $d_+ = 24.94$.

figure 15(*b*), it appears that the Strouhal number of the dominant shedding process is about $St = 0.103$, with occasional shedding at the higher frequency. As we will see in § 3.4, this higher frequency is not observed for the case of particles at the channel centre and therefore it can be conjectured to be the effect of the channel wall.

The two-time correlation of wall-normal force for the cases of $d_+ = 17.81$ and 24.94 at the channel centre are shown in figure 16. From the correlation, the Strouhal number of shedding for the two particles can be estimated as $St = 1/8.09 = 0.124$ and $St = 1/7.26 = 0.138$, which are in agreement with the Strouhal number of shedding for particles in isotropic turbulence (Bagchi & Balachandar 2003). Note that the increase in shedding frequency with increasing *Re* is consistent with results for a uniform ambient flow (Margavey & Bishop 1961; Sakamoto & Haniu 1990).

4.3. *Modelling of particle force*

In the modelling of force on a particle in a turbulent flow, it is appropriate to consider the interaction of incoming turbulent flow structures with the particle separately from the effect of vortex shedding. For a small particle, whose Reynolds number based on mean relative velocity is less than about 100, vortex shedding is generally absent, since the instantaneous Reynolds number remains below a threshold at all times. In the case of a stationary particle, this translates to the following approximate condition: $d_+ < 100/\langle u_+(y_{p+})\rangle$, and it applies over the entire channel cross-section. Such small particles can be treated essentially as point particles, and the instantaneous force on the particle can be reasonably well captured by standard drag correlation. This, however, requires complete information on the instantaneous undisturbed ambient fluid velocity at the particle location. Such information is readily available in a direct numerical simulation. The only challenge is for a particle located very close to the wall, in which case, as suggested by the experiments of Hall (1988) and Mollinger & Nieuwstadt (1996), the influence of lift force can become important even for such a small particle and must be appropriately modelled and included in force estimation.

In a Reynolds averaged Navier–Stokes (RANS) approach, only the mean ambient flow information is directly available. Provided the particle is small ($d_+ < 100/\langle u_+(y_{p+})\rangle$) the standard drag correlation is still adequate in predicting particle force (except perhaps very close to the wall, where the lift contribution can also be important). The time-varying turbulent velocity fluctuation seen by the particle must therefore be modelled. In order to recover accurately any non-zero mean wall-normal force, such models must capture appropriately the subtle correlation between streamwise and wall-normal velocity fluctuations. Furthermore, the model must account for the coupling between the different velocity components and the resulting disproportionate increase in wall-normal force fluctuation. Models of time history of velocity fluctuation seen by a particle in a turbulent flow have been developed primarily in the context of dispersion of fluid (tracer) and inertial particles. Models based on a modified Langevin equation have been shown to yield excellent result for the motion of fluid (tracer) particle wall-bounded flows (Illiopoulos & Hanratty 1999; Mito & Hanratty 2002). In comparison, investigations of fluid velocity fluctuations seen by an inertial particle in inhomogeneous turbulence are limited (see Thomson 1987; Reynolds 1997) and further work is required towards development of appropriate models suitable for wall-bounded flows.

A larger particle in the range $100 < d_+\langle u_+(y_{p+})\rangle < 200$ will exhibit occasional episodes of vortex shedding, whenever the instantaneous Reynolds number exceeds a threshold. During times when vortex shedding is absent, such a particle can be treated just as a small particle discussed above. For an even larger particle ($< d_+\langle u_+(y_{p+})\rangle < 200$) the shedding process is continually present at all times and must be accounted for in the force model. Most importantly, the force fluctuation arising from vortex shedding is not deterministically coupled to the ambient flow at the macroscale. Only a true DNS, which resolves the details of the flow around the particle at the microscale, such as those performed here, can yield the instantaneous force deterministically. In a point particle approach, even when the carrier phase turbulence is fully resolved with a DNS, the stochastic contribution from vortex shedding must be modelled. The best hope is to account for their statistical effect with a statistical model. The influence of the shedding process is strong in the transverse components of force (wall-normal and spanwise components in the present case). Its effect is relatively weak in the streamwise component. The shedding process occurs over a preferred frequency range and this must be factored into its model.

5. Conclusions

Here we performed direct numerical simulations of a turbulent channel flow over an isolated particle of finite size. These are fully resolved numerical simulations, where in addition to resolving the wide range of length and time scales associated with wall turbulence, all the length and time scales associated with the particle and the small-scale flow features generated by it are fully resolved. The undisturbed channel flow was modestly turbulent at $Re_\tau = 178.12$ and two different particle locations were considered within the channel: the first in the buffer region ($y_{p+} = 17.81$) and the second along the channel centreplane. A range of particle sizes was considered, from the smallest particle of diameter 3.56 in wall units to the largest particle of diameter 24.94 in wall units.

The key findings of this study are summarized in the following.

(i) Particles of size $d_+ < 100/\langle u_+(y_{p+})\rangle$ can be considered small and the instantaneous force on such particles is captured well with the standard drag formulation, provided the particle is away from the viscous sublayer. As the particle becomes within the viscous sublayer and approaches the wall, the lift contribution can be significant. We emphasize that the above finding is for a stationary particle.

(ii) For small particles within the buffer layer, the force fluctuation can be correlated well with incoming turbulent flow structures. The passage of low- and high-speed streaks over the particle yields streamwise force fluctuation. The turbulent ejection and sweep events as they pass over the particle contribute to wall-normal force fluctuation and similarly the presence of quasi-streamwise vortices close to the particle result in fluctuating spanwise force on the particle.

(iii) With increasing particle size, in the range $100 < d_+\langle u_+(y_{p+})\rangle < 200$, during periods of enhanced ambient flow when the instantaneous particle Reynolds number exceeds a threshold, episodic vortex shedding is observed. For even larger particles of $d_+\langle u_+(y_{p+})\rangle > 200$, vortex shedding is always present. The effect of vortex shedding is most clearly seen in the computed DNS wall-normal force component as large-amplitude quasi-periodic fluctuation. Corresponding fluctuation can be seen in the spanwise component as well, although the amplitude is weaker than in the wall-normal component. The streamwise component is not greatly influenced by the shedding process.

(iv) The shedding-induced force on the particle is fundamentally stochastic in nature and therefore cannot be predicted by any deterministic force law. In addition to the deterministic force contribution, a stochastic contribution is also required in order to appropriately account for the statistical effect of the shedding-induced force fluctuation.

(v) In all cases considered, the time-averaged mean streamwise force on the particle is more than an order of magnitude larger than the wall-normal component. The mean non-dimensional streamwise force steadily increases with particle size. Even for the largest particle under consideration, the mean streamwise force is reasonably well predicted by the standard drag correlation. A closer look at the data shows that for particles placed within the buffer layer, the computed DNS mean streamwise force is slightly, but consistently, higher than the prediction using the standard drag correlation. This increase in drag force is perhaps due to the added viscous effect of the nearby channel wall.

(vi) For a particle placed within the buffer layer, the computed DNS time-averaged wall-normal force is small, but remains negative (wallward) in all cases considered. This is in contrast to the strong positive lift force measured for a particle sitting on the wall within the viscous sublayer in the experiments of Hall (1988) and Mollinger & Nieuwstadt (1996). The importance of the lift force thus increases as the wall is approached. Here we observe that predictions, which include the lift contribution using the theoretical formulae proposed by Auton (1987) and Saffman (1965), and the empirical correlation proposed by Mei (1992) or Kurose & Komori (1999) are not able to capture the computed wall-normal force. The above lift formulae are based on a steady unbounded shear flow. Further investigation of lift force in a wall-bounded shear flow at finite *Re* is required.

(vii) Only for the smallest particle under consideration is the r.m.s. fluctuation in the wall-normal force extracted well with the standard drag correlation. With increasing particle size, the r.m.s. fluctuation in the wall-normal force progressively increases above what is predicted by the standard drag. For particles of size $d_+ = 10.69$, 17.81 and 24.94 placed at $y_{p+} = 17.81$, the under-prediction of r.m.s. wall-normal force fluctuation by standard drag is 25 %, 39 % and 51 %, respectively. The increased level of fluctuation is due to wake vortex shedding, whose effect has not been incorporated in the standard drag formulation. With increasing particle size, and correspondingly with increasing Reynolds number, the strength and extent of vortex shedding increase, and thus contribute to an increase in r.m.s. fluctuation.

(viii) The computed r.m.s. streamwise force fluctuation is lower than that predicted by the standard drag. Time history of the streamwise force shows that as the ambient turbulent flow passes over the particle, the frequency component of the fluctuation is reasonably well predicted, but the standard drag tends to overestimate the amplitude. For particles of size $d_+ = 10.69$, 17.81 and 24.94 placed at $y_{p+} = 17.81$, the over-prediction is by 25 %, 35 % and 32 %, respectively. Although, we are unable to pin-point the mechanistic origin for the reduced streamwise force fluctuation, it appears it is also related to increased particle Reynolds number and wake vortex shedding.

(ix) For a particle placed at the channel centre, the results can be compared with those from a particle subjected to isotropic turbulent crossflow (Bagchi & Balachandar 2003, 2004). Even for the largest particle, whose mean particle Reynolds number is 455, we observe the instantaneous streamwise force to be predicted reasonably well by standard drag correlation. This behaviour is due to the relatively low free-stream fluctuation (4 %) compared to the mean relative velocity in the present case. Based on the results of Bagchi & Balachandar (2003, 2004), we expect with increasing level of free-stream fluctuation for the larger particles, the computed streamwise force to depart significantly from the standard drag prediction. This will be of relevance for a free-moving particle, whose mean relative velocity will be much smaller than that of a particle frozen at the channel centre. Because of strong vortex shedding, the computed DNS wall-normal and spanwise forces exhibit large-amplitude quasi-periodic fluctuation.

This research was supported by the Center for the Simulation of Advanced Rockets at the University of Illinois at Urbana-Champaign through the US Department of Energy (subcontract number B341494) and by the Natonal Science Foundation through grant CBET-0639446. The National Center for Supercomputing Applications (UIUC) is also acknowledged, for the use of their computational facilities.

REFERENCES

AUTON, T. R. 1987 The lift force on a spherical body in a rotational flow. *J. Fluid Mech.* **183**, 199–218.

BAGCHI, P. & BALACHANDAR, S. 2002*a* Effects of free rotation on the motion of a solid sphere in linear shear flow at moderate *Re*. *Phys. Fluids* **14**, 2719–2737.

BAGCHI, P. & BALACHANDAR, S. 2002*b* Shear versus vortex-induced lift force on a rigid sphere at moderate *Re*. *J. Fluid Mech.* **473**, 379–388.

Bagchi, P. & Balachandar, S. 2003 Effect of turbulence on the drag and lift of a particle. *Phys. Fluids* **15**, 3496–3513.

Bagchi, P. & Balachandar, S. 2004 Response of the wake of an isolated particle to an isotropic turbulent flow. *J. Fluid Mech.* **518**, 95–123.

Bagchi, P., Ha, M. Y. & Balachandar, S. 2001 Direct numerical simulation of flow and heat transfer from a sphere in a uniform cross-flow. *Trans. ASME* I: *J. Fluids Engng* **123**, 347–358.

Brooke, J. W. & Hanratty, T. J. 1993 Origin of turbulence-producing eddies in a channel flow. *Phys. Fluids* A**5**, 1011–1022.

Brooke, J. W., Hanratty, T. J. & McLaughlin, J. B. 1994 Free flight mixing and deposition of aerosols. *Phys. Fluids* **6**, 3404–3415.

Brucato, A., Grisafi, F., & Montante, G. 1998 Particle drag coefficients in turbulent fluids. *Chem. Engng Sci.* **53**, 3295–3314.

Caraman, N., Boree, J. & Simonin, O. 2003 Effect of collisions on the dispersed phase fluctuation in a tube 1flow: experimental and theoretical analysis. *Phys. Fluids* 1**15**, 3602–3612.

Chakraborty, P., Balachandar, S. & Adrian, R. J. (2005) On the relationships between local vortex identification schemes. *J. Fluid Mech.* **535**, 189–214.

Christensen, K. T. & Adrian, R. J. 2001 Statistical evidence of hairpin vortex packets in wall turbulence. *J. Fluid Mech.* **431**, 433–443.

Crowe, C. T., Sommerfeld, M., & Tsuji, Y. 1998 Multiphase flows with droplets and particles. CRC Press. New York.

Dandy, D. S. & Dwyer, H. A. 1990 A sphere in shear flow at finite Reynolds number: effect of shear on particle lift, drag and heat transfer. *J. Fluid Mech.* **216**, 381–410.

Deville, M. O., Fischer, P. F. & Mund, E. H. 2002 High-order methods for incompressible fluid flow. Cambridge University Press.

Fessler, J. R., Kulick, J. D. & Eaton, J. K. 1994 Preferential concentration of heavy particles in a turbulent channel flow. *Phys. Fluids* **6**, 3742–3749.

Gore, R. A. & Crowe, C. T. 1990 Discussion of particle drag in a dilute turbulent two-phase suspension flow. *Intl J. Multiphase Flow* **16**, 359–361.

Hall, D. 1988 Measurements of the mean force on a particle near a boundary in turbulent flow. *J. Fluid Mech.* **187**, 451–466.

Illiopoulos, I. & Hanratty, T. J. 1999 Turbulent dispersion in a non-homogeneous field. *J. Fluid Mech.* **392**, 45–71.

Johnson, T. A. & Patel, V. C. 1999 Flow past a sphere up to Reynolds number of 300. *J. Fluid Mech.* **378**, 19–70.

Kaftori, D., Hetsroni, G. & Banerjee, S. 1995*a* Particle behavior in the turbulent boundary layer: I. Motion, deposition and entrainment. *Phys. Fluids* **7**, 1095–1106.

Kaftori, D., Hetsroni, G. & Banerjee, S. 1995*b* Particle behavior in the turbulent boundary layer: II. Velocity and distribution profiles, deposition and entrainment. *Phys. Fluids* **7**, 1107–1121.

Kim, J., Moin, P. & Moser, R. D. 1987 Turbulence statistics in fully developed channel flow at low Reynolds number. *J. Fluid Mech.* **177**, 133–166.

Kurose, R. & Komori, S. 1999 Drag and lift forces on a rotating sphere in a linear shear flow. *J. Fluid Mech.* **384**, 183–206.

McLaughlin, J. B. 1991 Inertial migration of a small sphere in linear shear flows. *J. Fluid Mech.* **224**, 261–274.

Margavey, R. H. & Bishop, R. L. 1961 Transition ranges for three dimensional wakes. *Can. J. Phys.* **39**, 1418–1422.

Mei, R. 1992 An approximate expression for the shear lift force on a spherical particle at finite Reynolds number. *Intl J. Multiphase Flow* **18**, 145–147.

Mei, R. 1994 Effect of turbulence on the particle settling velocity in the nonlinear drag range. *Intl J. Multiphase Flow* **20**, 273–284.

Mei, R. & Adrian, R. 1992 Flow past a sphere with an oscillation in the free-stream velocity and unsteady drag at finite Reynolds number. *J. Fluid Mech.* **237**, 323–341.

Merle, A., Legendre, D. & Magnaudet, J. 2005 Forces on a high–Reynolds–number spherical bubble in a turbulent flow. *J. Fluid Mech.* **532**, 53–62.

Mito, Y. & Hanratty, T. J. 2002 Use of a modified Langevin equation to describe turbulent dispersion of fluid particles in a channel flow. *Turbulence Combust.* **68**, 1–26.

Mittal, R. 2000 Response of the sphere wake to free–stream fluctuations. *Theoret. Comput. Fluid Dyn.* **13**, 397–419.

Mollinger, A. M. & Nieuwstadt, F. T. M. 1996 Measurement of the lift force on a particle fixed to the wall in the viscous sublayer of a fully developed turbulent boundary layer. *J. Fluid Mech.* **316**, 285–306.

Moore, D. W. 1963 The boundary layer on a spherical gas bubble. *J. Fluid Mech.* **16**, 161–176.

Moore, D. W. & Saffman, P. G. 1968 The rise of a body through a rotating fluid in a container of finite length. *J. Fluid Mech.* **31**, 635–642.

Natarajan, R. & Acrivos, A. 1993 The instability of the steady flow past spheres and disks. *J. Fluid Mech.* **254**, 323–344.

Pan, Y. & Banerjee, S. 1996 Numerical simulation of particle interactions with wall turbulence. *Phys. Fluids* **8**, 2733–2755.

Pan, Y. & Banerjee, S. 1997 Numerical investigations of the effects of large particles in wall turbulence. *Phys. Fluids* **9**, 3786–3807.

Ranz, W. E. & Marshall, W. R. 1952 Evaporation from drops. *Chem. Engng Prog.* **48**, 141–146.

Rashidi, M., Hetsroni, G. & Banerjee, S. 1990 Particle turbulence interaction in a boundary layer. *Intl J. Multiphase Flow* **16**, 935–949.

Reynolds, A. M. 1997 On the application of Thompson's random flight model to prediction of particle dispersion within a ventilated airspace. *J. Wind Engng Indust. Aerodyn.* **67–68**, 627–638.

Rudolff, R. R. & Bachalo, W. D. 1988 Measurement of droplet drag coefficients in polydispersed turbulent flow field. *AIAA Paper* 88-0235.

Saffman, P. G. 1965 The lift on a small sphere in a slow shear flow. *J. Fluid Mech.* **22**, 385–400.

Sakamoto, H. & Haniu, H. 1990 A study of vortex shedding from spheres in a uniform flow. *Trans. ASME* I: *J. Fluids Engng* **112**, 386–392.

Sato, Y. & Hishida, K. 1996 Transport process of turbulence energy in particle–laden turbulent flow. *Intl J. Heat Fluid Flow* **17**, 202–210.

Schiller, L. & Neumann, A. 1933 Uber die grundlegenden berechungen bei der schwerkraftaufberereitung. *Z. Vereines Deutsch. Ingen.* **77**, 318–320.

Sirignano, W. A. 1999 Fluid dynamics and transport of droplets and sprays. Cambridge University Press.

Suzuki, Y., Ikenoya, M. & Kasagi, N. 2000 Simultaneous measurement of fluid and dispersed phases in a particle–laden turbulent channel flow with the aid of 3-D PTV. *Exps. Fluids* **29**, s185–s193.

Thompson, D.J. 1987 Criteria for the selection of stochastic models of particle trajectories in turbulent flows. *J. Fluid Mech.* **180**, 529–556.

Tomboulides, A. G. & Orszag, S. A. 2000 Numerical investigation on transitional and weak turbulent flow past a sphere. *J. Fluid Mech.* **416**, 45–73.

Torobin, L. B. & Gauvin, W. H. 1959 Fundamental aspects of solid–gas flow. *Can. J. Chem. Engng* **38**, 129.

Tsuji, Y. & Morikawa, Y. 1982 LDV measurements of an air–solid two-phase flow in a horizontal pipe. *J. Fluid Mech.* **120**, 385–409.

Tsuji, Y., Morikawa, Y. & Shiomi, H. 1984 LDV measurements of an air–solid two-phase flow in a vertical pipe. *J. Fluid Mech.* **139**, 417–434.

Uhlherr, P. H. T. & Sinclair, C. G. 1970 The effect of freestream turbulence on the drag coefficients of spheres. *Proc. Chem.* **1**, 1.

Vasseur, P. & Cox, R. G. 1977 The lateral migration of spherical particles sedimenting in a stagnant bounded fluid. *J. Fluid Mech.* **80**, 561–591.

Wakaba, L. & Balachandar, S. 2005 History force on a sphere in a weak linear shear flow. *Intl J Multiphase Flow* **31**, 996–1014.

Wu, J. S. & Faeth, G. M. 1994 Sphere wakes at moderate Reynolds numbers in a turbulent environment. *AIAA J.* **32**, 535–541.

Young, J. B. & Hanratty, T. J. 1991 Optical studies on the turbulent motionsx of solid particles in a pipe flow. *J. Fluid Mech.* **231**, 665–688.

Zarin, N. A. & Nicholls, J. 1971 Sphere drag in solid rockets – non–continuum and turbulence effects. *Combust. Sci. Technol.* **3**, 273.

Zeng, L. 2007 Interaction of a finite-size particle with wall turbulene. PhD thesis, University of Illinois, Urbana, IL.

Zeng, L. Balachandar, S. & Fischer 2005 Wall-induced forces on a rigid sphere at finite Re. *J. Fluid Mech.* **536**, 1–25.

Zhou, J., Adrian, R. J., Balachandar, S. & Kendall, T. M. 1999 Mechanisms for generating coherent packets of hairpin vortices in channel flow. *J. Fluid Mech.* **387**, 353–396.